Journal of Extracellular Vesicles

RESEARCH ARTICLE OPEN ACCESS

Hypoxic Neural Stem Cells Enhance Spinal Cord Repair Through HIF-1a/RAB17-Driven Extracellular Vesicle Release

Tian Qin[1,2,3,4] | Yiming Qin[1,2,3,4] | Haicheng Wen[1,2,3,4] | Tianding Wu[1,2,3,4] | Chunyue Duan[1,2,3,4] | Yong Cao[1,2,3,4] | Yi Sun[1,2,3,4] | Hongkang Zhou[5] | Hongbin Lu[2,3,4,6] | Liyuan Jiang[1,2,3,4] | Jianzhong Hu[1,2,3,4] | Chengjun Li[2,3,4,6]

[1]Department of Spine Surgery and Orthopaedics, Xiangya Hospital, Central South University, Changsha, China | [2]Key Laboratory of Organ Injury, Aging and Regenerative Medicine of Hunan Province, Changsha, China | [3]Hunan Engineering Research Center of Sports and Health, Changsha, China | [4]National Clinical Research Center for Geriatric Disorders, Xiangya Hospital, Central South University, Changsha, China | [5]Central South University Institute for Advanced Study, Changsha, China | [6]Department of Sports Medicine, Xiangya Hospital, Central South University, Changsha, China

Correspondence: Liyuan Jiang (jiangliyuanxy@csu.edu.cn) | Jianzhong Hu (jianzhonghu@csu.edu.cn) | Chengjun Li (chengjunli@csu.edu.cn)

Received: 6 January 2025 | **Accepted:** 11 June 2025

Funding: This study was funded by the National Natural Science Foundation of China (Grant number 82030071), Changsha Science and Technology Project (Grant number kh2103008), Hunan Province Graduate Research Innovation Project (Grant number CX20230379), Natural Science Foundation Project of Hunan Province (Grant number 2024JJ6637), Natural Science Foundation Project of Changsha (Grant number kq2403018), Youth Fund Scientific Research Project of Xiangya Hospital (Grant number 2023Q05).

Keywords: CAQK/Angiopep2 peptides | extracellular vesicles | hypoxia | neural stem cells | spinal cord injury

ABSTRACT

Spinal cord injury (SCI) is a severe and complex condition that can lead to significant physical impairments and affect the life quality of patients. Neural stem cells (NSCs) transplantation holds as a promising therapeutic approach for SCI. However, the challenging post-SCI microenvironment limits NSCs effectiveness. Our current research has found that transplanted NSCs, though with lower survival and differentiation, still aided in injury repair. Hypoxia was identified as a stressor inducing the release of extracellular vesicles (EVs) from NSCs through HIF-1α/RAB17 enhancing SCI repair. By extracting and modifying these EVs derived from hypoxia treated NSCs with CAQK/Angiopep2 peptides, we were able to accurately deliver them to the injury site, enhancing recovery without relying on cell survival or differentiation. This study delved into the reparative role and underlying mechanisms of transplanted NSCs in SCI, focusing on their non-cellular contributions and developed an innovative, targeted strategy for the transplantation of EVs derived from NSCs, offering a cell-free, precision therapeutic intervention for the treatment of SCI.

1 | Introduction

Spinal cord injury (SCI) typically led to permanent functional loss. As an acute traumatic injury to the central nervous system, SCI leads to the destruction of axonal network and blood vessels. Following trauma, the secondary injury could induce destabilization of the local microenvironment and trigger an excessive inflammatory cascade, which initiates a chain of events culminating in neuronal apoptosis and severely impaired axonal regeneration capacity (Ahuja et al. 2017; Hu et al. 2023). The treatment of SCI, as a global challenge, urgently requires the exploration of active and effective treatment methods (GBD 2016 2019).

Tian Qin and Yiming Qin contributed equally to this work.

This is an open access article under the terms of the Creative Commons Attribution-NonCommercial-NoDerivs License, which permits use and distribution in any medium, provided the original work is properly cited, the use is non-commercial and no modifications or adaptations are made.

© 2025 The Author(s). *Journal of Extracellular Vesicles* published by Wiley Periodicals LLC on behalf of International Society for Extracellular Vesicles.

The cell-based therapy is widely regarded as a revolutionary approach in the treatment of SCI (Ribeiro et al. 2023). Neural stem cells (NSCs) are multipotent progenitors capable of generating neurons and microglia, which are essential for maintaining complex sensory and cognitive functions in the nervous system, making NSCs a promising candidate for SCI treatment (Hosseini et al. 2024; Huang et al. 2022). However, the limitations and challenges associated with direct transplantation of NSCs into target tissues cannot be ignored (Yang et al. 2024; Zeng 2023). Although NSC transplantation is known to be an effective therapy for SCI treatment, previous studies have shown that the survival rate of transplanted stem cells is low, and long-term detection reveals a tendency toward astrocyte differentiation (Xue et al. 2021). This indicates that NSC transplantation may promote functional recovery after SCI through means other than neural differentiation.

Extracellular vesicles (EVs) are nano-sized lipid vesicles that originate from the inward budding of the endosomal membrane and represent a significant cell-derived component, formed by the multivesicular body and are released into the extracellular space by fusion with the plasma membrane, protecting their contents from degradation (Hill 2019; van Niel et al. 2018). EVs mediate intercellular communication through the transfer of diverse bioactive cargo, including genetic material, proteins, and lipid mediators that regulate recipient cell functions. EVs not only have cell-type-specific proteins but also have a set of common and abundant proteins, including CD9, CD63, CD81 and TSG101 (Xu et al. 2016). The specific surface ligands of EVs ensure their binding to target cells and the delivery of their contents, thus regulating specific biological functions, including intercellular signalling, angiogenesis, tumour cell proliferation and metastasis and immune regulation (Kumar et al. 2024). In recent years, researches focused on the applications of stem cell-derived EVs in tissue engineering, inflammation regulation, regenerative medicine and other fields are emerging as the replacement therapy of stem cell transplantation (Liu et al. 2021; Zhang et al. 2016; Zhou et al. 2024). Therefore, exploring the potential mechanisms of NSC therapy for SCI is beneficial for us to discover new therapeutic approaches for SCI.

Hypoxia serves as a pathological hallmark of multiple severe disorders and frequently manifests as a secondary complication following SCI. Hypoxia can occur as a result of various factors, such as blood loss, respiratory failure, or vascular damage. Severe hypoxia could lead to neuronal death, inflammation, and tissue damage, impairing the recovery process and delay functional improvement in patients with SCI (Lee et al. 2005; Chen et al. 2024). However, there are also studies indicating that a certain degree of hypoxia can play a positive role in tissue damage repair. Hypoxia activates the hypoxia inducible factor (HIF) signalling pathway (Semenza 2000; LaGory and Giaccia 2016). Under normoxic conditions, HIF-1α is rapidly hydroxylated by prolyl-4-hydroxylases and directed to proteasomal degradation. When hypoxia happens, this degradation process is suppressed, and the HIF-α subunits translocate into the nucleus to bind with HIF-1β. The heterodimeric complex then locates to the hypoxia-responsive elements leading to the subsequent upregulation of more than 100 target genes including vascular growth factors such as VEGF-A and PDGF-B to promote tissue survival (Rattner et al. 2019; Schito et al. 2012). Although preclinical studies consistently demonstrate the potential of NSC-transplantation for neural functional repair after SCI, the hypoxic microenvironment in the core area of the injury significantly reduces the survival rate of transplanted cells. The current research paradigm mainly focuses on the direct neural differentiation potential of transplanted stem cells, but systematically ignores its paracrine effect-especially the neurovascular regeneration mechanism mediated by EVs secreted by NSCs under hypoxic stress.

In this research, we systematically investigated the molecular mechanisms underlying the release of EVs from NSCs under hypoxic conditions and characterized the expression profile of hypoxia-induced NSC-EVs, uncovering the key mediating role of EVs in the treatment of SCI by NSCs transplantation. Using a double targeted peptides labelling methods to modify EVs for precise administration, this research provided an effective treatment method for SCI using hypoxic NSCs-EVs.

2 | Materials and Methods

2.1 | Animals

C57BL/6-Tg(CAG-EGFP)1Osb/J mice were obtained from the Jackson Laboratory (#003291) (Okabe et al. 1997), which we abbreviated them as "EGFP mice". All animal experiments performed in this study were previously authorized by the Ethics Committee of Central South University for Scientific Research. Mice were bred in Department of Laboratory Animals of Central South University under SPF (specific pathogen-free) conditions (Specific reference is made to the Chinese national standard GB/T14925), with a 12 h light-dark cycle, room temperature of 22–24°C and ad libitum access to food and water. All procedures were conformed with the Helsinki Declaration and approved by the Xiangya Hospital Medical Ethics Committee of Central South University (XY20240105008).

2.2 | Complete Transection SCI Model Construction and Treatment

To exclude the influence of severe urinary retention on the observation and evaluation of the repair effect of the SCI mice, female mice were selected owing to their shorter and more accessible urethra, which facilitates urination (in contrast, the narrower and longer urethra in male mice causes urination difficulties and higher mortality) (Okabe et al. 1997). Eight-week-old female C57BL/6J mice were randomly divided into designated groups (complete transection SCI model: Sham vs. Control vs. NSCs, eight animals per group; NSCs vs. shNC-NSCs vs. shRab17-NSCs, six animals per group). Mice were conducted laminectomy and the 10th thoracic (T10) spinal cord was exposed after deep anaesthesia by isoflurane inhalation. For mice in sham group, T10 laminectomy without spinal cord transection was conducted. For the complete transection SCI model, a transection of spinal cord centred at T10 with ~2 mm in length was made using microscissors. The block of spinal cord was removed and the matrigel scaffold with or without NSCs was implanted after complete haemostasis. Briefly, neurospheres were collected and dissociated into single cells using accutase (Gibco). After centrifugation,

20013078, 2025, 7, Downloaded from https://isevjournals.onlinelibrary.wiley.com/doi/10.1002/jev2.70126 by CochraneChina, Wiley Online Library on [27/07/2025]. See the Terms and Conditions (https://onlinelibrary.wiley.com/terms-and-conditions) on Wiley Online Library for rules of use; OA articles are governed by the applicable Creative Commons License

NSCs were resuspended into Matrigel (Corning) at a density of approximately 100,000 cells/μL. Mixture was divided into 10 μL/scaffold and incubated at 37°C for 30 min for solidification. After incubation, scaffolds with or without NSCs were implanted into the surgery site after complete haemostasis. After surgery, mice were administered with penicillin (3000 IU/mL) in the water for 3 days and their bladders were manually emptied every 2 days until urinating function was recovery. The SCI mice received Buprenorphine (0.03 mg/kg/day, subcutaneous injection) to alleviate pain during the first week after surgery.

2.3 | Contusion SCI Model Construction and Treatment

The contusion SCI was constructed using a modified Allen's weight-drop apparatus (weight: 10 g, vertical height: 20 mm; contusion SCI model: Sham vs. Control vs. NormoNSCs-EVs vs. HypoNSCs-EVs vs. CAQK-Angiopep2-HypoNSCs-EVs, 10 animals per group). Briefly, mice were conducted laminectomy and the 10th thoracic (T10) spinal cord was exposed after deep anaesthesia by isoflurane inhalation. For mice in sham group, T10 laminectomy without spinal cord contusion was conducted. Following the modified Allen's method, a 10 g impactor rod struck vertically from a height of 2.5 cm. For treatment, the EVs were extracted from the wild-type C57BL/6J embryos (E16-18) derived NSCs under normoxic or hypoxic conditions for 18 h. And the hypoNSCs-EVs were modified with DSPE-PEG2000-CAQK and DSPE-PEG2000-Angiopep2 for target delivery. After SCI, the normoNSCs-EVs, hypoNSCs-EVs CAQK-Angiopep2-HypoNSCs-EVs and equal volume of normal saline were administered via tail vein injection (100 μg per mouse, once every 2 days, and continuous intervention for 1 month). After surgery, mice were administered with penicillin (3000 IU/mL) in the water for 3 days and their bladders were manually emptied every 2 days until urinating function was recovery. The SCI mice received Buprenorphine (0.03 mg/kg/day, subcutaneous injection) to alleviate pain during the first week after surgery.

2.4 | Primary NSCs Culture

The primary NSCs were prepared and cultivated as previously described (Lu et al. 2012) Specifically, we extracted NSCs from the spinal cords of embryonic Day 16–18 (E16-18) C57BL/6J mice or EGFP mice. The spinal cords were carefully dissected, followed by removal of the dura mater. Subsequently, the isolated tissues were sectioned into fragments measuring approximately 1 mm^3. The pieces were trypsinized for 15 min at 37°C (Gibco). After filtered by a 40 μm cell filter, the cells were centrifuged and resuspended in NSC growth medium containing Neurobasal-A (Gibco), 0.24% GlutaMAX supplement (Gibco), 2% B-27 supplement (Gibco, 17504044), 20 ng/mL EGF (Novoprotein) and 20 ng/mL FGFb (Novoprotein, P15655). Cells were seeded and cultivated for 5–7 days. After centrifugation, neurospheres were dissociated into single cells using accutase (Gibco) and passage into further generation. For NSCs tracing post transplantation, we used two distinct approaches based on the experimental objectives: (1) To observe the fate of transplanted NSCs, we labelled EGFP-NSCs with PKH26 dye for generating PKH26-EGFP dual-labelled NSCs. (2) To investigate the uptake of EVs released by transplanted NSCs by surrounding cells, we transfected NSCs isolated from wild-type mice with CD63-copGFP-Flag lentivirus.

2.5 | Cell Tracing for PKH26 and EGFP Dual-Labelled NSCs Post Transplantation

Primary NSCs were isolated from the cortical tissue of EGFP transgenic mice. Following expansion and culture, neurospheres were enzymatically dissociated into single-cell suspensions using Accutase (Gibco). Approximately 2×10^7 cells were resuspended in serum-free medium, transferred to a conical-bottom polypropylene tube, and centrifuged (400 × *g*, 5 min) to form a loose pellet. The pellet was gently resuspended in 1 mL Diluent C (Sigma) to generate a 2× Cell Suspension. Concurrently, a 2× Dye Solution was prepared by combining 4 μL PKH26 ethanolic dye (Sigma) with 1 mL Diluent C in a polypropylene tube, followed by thorough mixing. The 2× Cell Suspension was rapidly added to the 2× Dye Solution, and the mixture was homogenized by pipetting. After 3 min of incubation with intermittent agitation, staining was terminated by adding 2 mL 1% BSA solution (1:1 v/v). Cells were pelleted by centrifugation (400 × *g*, 5 min), and unbound dye was removed through three sequential washes with 10 mL complete medium. Finally, PKH26-labelled EGFP+ NSCs were transplanted into the lesion site of SCI mice as previously described.

2.6 | Primary Brain Microvascular Endothelial Cells (BMECs) Culture and In Vivo Angiogenesis Analysis

Primary BMECs were prepared as previously described (You et al. 2023). Briefly, 6-week-old C57BL/6J mice were sacrificed and the brains were dissected immediately and immerged in Hank's balance salt solution (HBSS, Procell). The meninges, big vessels and white matter were removed, remaining the cerebral cortices. Cortices were cut into small pieces of approximately 1 mm^3 and digestive with 1 mg/mL collagenase II (Sigma–Aldrich) and 0.2 mg/mL DNAse I (Sigma–Aldrich) for 1.5 h at 37°C. Uniform suspension was washed twice using HBSS. Pellet was then resuspended in HBSS containing 20% bovine serum albumin (BSA) and centrifuged at 1500 *g* for 15 min to remove the myelin debris. The microvascular segments were digestive again with 1 mg/mL collagenase/dispase (Sigma–Aldrich) and 0.2 mg/mL DNAse I (Sigma–Aldrich) for 1 h at 37°C. After centrifugation, cells were resuspended in primary mouse BMECs medium containing Dulbecco's modified Eagle's medium (DMEM) (1 g/mL glucose, Gibco), 20% foetal bovine serum (NEWZERUM), 100 μg/mL heparin sodium (MCE), 20 ng/mL FGFb (Novoprotein), with 2 ug/mL puromycin (MCE), and seeded in type I collagen (Sigma–Aldrich)-coated plate. After 48 h, medium was replaced with fresh medium without puromycin. Matrigel angiogenesis assay in vivo was conducted according to a previously described procedure (Zhou et al. 2019). Briefly, approximately 1×10^6 primary BMECs with NSCs-culture medium (The NSC-conditioned medium was mixed with the primary microglial cell culture medium at a 1:1 (v/v) ratio) or EVs (100 μg/mL) were suspended in 100 μL Matrigel. Mice were subcutaneously injected with the BMECs-Matrigel mixtures. Mixtures with treated BMECs, untreated BMECs or PBS (blank control) were injected to different positions

20013078, 2025, 7, Downloaded from https://isevjournals.onlinelibrary.wiley.com/doi/10.1002/jev2.70126 by CochraneChina, Wiley Online Library on [27/07/2025]. See the Terms and Conditions (https://onlinelibrary.wiley.com/terms-and-conditions) on Wiley Online Library for rules of use; OA articles are governed by the applicable Creative Commons License

of the same mouse. After 7 days, mixtures were dissected and photographed by camera (Nikon D7100) immediately, and then fixed and sliced for CD31 immunostaining to quantify the density of formed microvessels.

2.7 | BV2 Cell Line Culture

Immortalised murine microglial (BV2, procell) cell line was cultivated in DMEM containing 10% FBS and 1% Penicillin/Streptomycin (procell). All cell lines were cultivated at 37°C and 5% CO_2. LPS is the most common in vitro intervention method for activating microglia and is used in various SCI-related studies (John et al. 2025; Chen et al. 2024; Wang et al. 2023). To establish an in vitro model of the inflammatory microenvironment after SCI, the BV2 microglial cell line was stimulated with 100 μg/mL lipopolysaccharide (LPS) to induce an inflammatory activation state. Based on this inflammatory model, the experimental group adopted the following intervention strategies: (1) NSC-conditioned medium intervention: The NSC-conditioned medium was mixed with the primary microglial cell culture medium at a 1:1 (v/v) ratio. (2) EV intervention: Referring to the results of the previous dose-response experiment, a 100 μg/mL EVs concentration was used for co-culture, and this concentration have demonstrated significant biological efficacy in prior experimental validation (Qin et al. 2024). And 24 h incubation, the cells were harvest for further analysis.

2.8 | Primary Hippocampus Neurons Culture

The primary hippocampus neurons were isolated as previously described (Festa et al. 2023). In brief, E16-18 embryos were dissociated from pregnant C57BL/6J mice. The brains were isolated and the dura was removed. Hippocampus was then dissected anatomically and cut into pieces of approximately 1 mm^3. Tissue was trypsinized for 10 min at 37°C and gently triturated. After filtered by a 40 μm cell filter, the cells were centrifuged and resuspended into primary neuron growth medium containing Neurobasal-A (Gibco), 1% GlutaMAX supplement (Gibco), 2% B-27 supplement (Gibco). Subsequently, cells were seeded on poly-D-lysine-coated plates (Sigma–Aldrich) and cultivated for 7–10 days. For intervention, the NSCs-culture medium (NSC-conditioned medium was mixed with the neural culture medium at a 1:1 (v/v) ratio) or EVs (100 μg/mL) were add to the neural cell culture system, and incubated for 3 days.

2.9 | Hypoxic Cultivation of NSCs In Vitro

After passaging into the third generation, NSCs were cultivated in normoxic cultivation condition (37°C, 5% CO_2) for 4 h to restore homeostasis and then put into anaerobic workstation (Don Whitley Scientific) for 6, 12, 18, 24 or 48 h. After anaerobic cultivation, neurospheres were imaged by light microscope and harvested for total RNA or protein extraction.

2.10 | Apoptosis Detection of Transplanted NSCs

Apoptosis of transplanted NSCs was detected by one-step TUNEL In Situ Apoptosis Kit (Elabscience, Elab Fluor 647) according to the user's manual. Specifically, frozen sections were fixed by 4% polyformaldehyde for 30 min and washed in PBS three times. Sections were incubated with PBS containing 0.5% Triton X-100 (BioFroxx) for 5 min at room temperature. After washing with PBS, TUNEL detection solution (mixture of terminal deoxynucleotidyl transferase enzyme and Elab Fluor 647-labelled dUTP) was added on sections and incubated avoid light at 37°C for 60 min. Ultimately, apoptosis of implemented NSCs was examined using fluorescence microscope (Zeiss ApoTome.2).

2.11 | Hypoxia Detection of Transplanted NSCs

Hypoxia state of transplanted NSCs in the SCI site was detected using Hypoxyprobe Kit (Hypoxyprobe, Inc) following the user's manual. Specifically, after 0 or 24 h of NSCs implementation, mice received intraperitoneal administration of Solid pimonidazole HCl (Hypoxyprobe-1) at a dosage of 1.5 mg/mouse. After 60 min, spinal cords were harvested and fixed. For immunofluorescence detection of Hypoxyprobe, frozen sections were incubated with anti-pimonidazole antibody (1:500) overnight at 4°C and washed three times with PBS. Sections were incubated with ATTO 594-conjugated monoclonal antibody (1:200) for 2 h at room temperature and imaged by fluorescence microscope (Zeiss ApoTome.2).

2.12 | EVs Extraction and Characteristic

NSCs was cultivated under normoxic or hypoxic condition for 18 h and the supernatants were collected to isolate the normoNSCs-EVs or hypoNSCs-EVs according to the differential centrifugation/ultracentrifugation protocols (Chen et al. 2018). Specifically, supernatants were centrifuged at 300 × *g* for 10 min, 3000 × *g* for 30 min and 10,000 × *g* for 30 min and the pellet was discarded to remove cellular debris. The remaining supernatants were then ultracentrifuged at 100,000 × *g* for 2 h and the pellets were retained and washed in PBS at 100,000 × *g* for another 2 h. The ultimate pellets, which was the EVs, were resuspended in PBS. The EVs were characterized by transmission electron microscopy (TEM, FEI company, USA) for morphological analysis. Nanoparticle tracking analysis (NTA) was performed on Nanoparticle Tracking Analyzer (ZetaView, Particle Metrix, Germany) using EVs from 50 mL culture medium suspended in 1.5 mL PBS.

2.13 | Immunofluorescence

Spinal cords were dissected after cardiac perfusion with 4% paraformaldehyde and sections were obtained with thickness of 16 μm using cryostat (Thermo Fisher Scientific). For immunofluorescence, slices were washed three times in PBS, permeabilized with 0.1% Triton X 100 for 15 min and blocked with 5% BSA for 30 min. Primary antibodies (**Table S1**) were diluted and incubated with slices overnight at 4°C. After washing three times with PBS, slices were incubated with corresponding fluorescence

20013078, 2025, 7, Downloaded from https://isevjournals.onlinelibrary.wiley.com/doi/10.1002/jev2.70126 by CochraneChina, Wiley Online Library on [27/07/2025]. See the Terms and Conditions (https://onlinelibrary.wiley.com/terms-and-conditions) on Wiley Online Library for rules of use; OA articles are governed by the applicable Creative Commons License

secondary antibodies (Abcam) at room temperature for 1.5 h. Subsequently, mounting medium containing DAPI (GeneTex) was used to stain the nucleus and seal the slices with coverslips. Finally, slices were imaged by fluorescence microscope (Zeiss ApoTome.2).

2.14 | Transmission Electron Microscopy (TEM)

The NSCs cultured in vitro (hypoxic and non-hypoxic treatment groups) were centrifuged (300 × *g* for 5 min) to obtain cell pellet masses. After pre-fixation with 2.5% glutaraldehyde and post-fixation with 1% osmium tetroxide, the cell pellet masses should not be dispersed to achieve the morphological stability of the cell membrane and organelles. Then, 70–90 nm ultrathin sections were prepared after gradient ethanol dehydration and epoxy resin infiltration and embedding. The contrast was enhanced by double staining with uranyl acetate and lead citrate. The subcellular structures such as multivesicular bodies (MVBs) were observed under high-resolution imaging at an accelerating voltage of 80 kV (10,000× and 20,000×). The typical characteristics of MVBs are a cavity wrapped by a double membrane with a diameter of 200–500 nm, containing 10–50 intracavitary vesicles with a medium electron density.

2.15 | 3D-τ-STED/STED-FLIM

To validate the colocalization of RAB17 and CD63 molecules in NSCs, NSCs were dissociated using accutase and seeded on poly-D-lysine-coated coverslips (0.17 μm). After incubation at 37°C for 30 min, NSCs were fixed, immunostained for RAB17 and CD63, and coverslipped with Prolong Diamond Antifade Mounting Medium (Thermo Fisher Scientific). Subsequently, NSCs were imaged with Leica STELLARIS 8 Stimulated emission depletion (STED) microscope using the ×100 objective (1.4 NA oil) (Leica Microsystems). To improve the signal to noise ratio, STED microscope with Fluorescence Lifetime Imaging (STED-FILM) were performed using the tauSTED mode at a fluorescence lifetime range from 0.5 to 8 ns. Pixel size was limited to less than 30 nm and thickness of z-stack was set to 0.25 μm.

2.16 | Flow Cytometry

The spinal tissues were dissected from the SCI mice after removing surrounding meninges. Briefly, the remained tissues were pipetted until tissue pieces were digested into single cells using 0.25% Collagenase A (Roche, United States) and 0.1% Dispase II (Sigma). After washing, cells were resuspended in PBS with 2 mM EDTA (Thermo Fisher Scientific). and 1 μg/mL 4–6, Diamidino-2-Phenylindole (DAPI, BD Biosciences). The sample was sorted using a FACS Aria II SORP cell sorter (BD Biosciences) cytometer, and the $DAPI^+$ cells and doublets were excluded during the analysis. For EVs flowcytometry analysis, a 100 kD filtration membrane was used to enrich the labelled EVs, and the fluorescence labelling efficiency of the EVs were detected with Cytek Northern Lights. All the data were then analysed utilizing FlowJo software (TreeStar).

2.17 | Western Blot

Total protein was extracted from NSCs under hypoxic cultivation, NSCs transfected with shRAB17 lentivirus and BV2 cells treated with condition medium or EVs from NSCs, using RIPA lysis buffer (Beyotime) with protease inhibitor cocktail (Beyotime). Concentration of total protein was detected using BCA protein assay kit (Multisciences) according to the manufacture's protocol. Protein samples with equal amounts (5 μL/well, 2 μg/μL) were separated by 10% sodium dodecyl sulphate-polyacrylamide gel electrophoresis and were transferred onto PVDF membranes. Blots were blocked by 5% milk (diluted in TBST) for 2 h and incubated with antibodies followed by incubation with HRP-conjugated secondary antibody at room temperature for 120 min (**Table S1**). After washed three times with TBST, blots were visualized using an enhanced chemiluminescence (ECL) kit (ShareBio).

2.18 | RNA Extraction, Library Preparation and Sequencing

Total RNA from NSCs under hypoxic or normoxic cultivation ($n = 3$ per experimental group, each sample was collected from a 75 cm^2 culture plate), with all samples originating from the same production batch) was extracted using TRIzol Reagent (Ambion). DNA was digested by DNase I. After RNA quality and integrity determination, qualified RNA (RNA Integrity Number (RIN) ≥ 7.0) was quantified by Qubit3.0 with QubitTM RNA Broad Range Assay kit (Life Technologies). Stranded RNA sequencing library was prepared using 2 μg total RNA via KC-DigitalTM Stranded mRNA Library Prep Kit for Illumina (Wuhan Seqhealth Co., Ltd. China) following the manufacturer's protocol. Unique molecular identifier (UMI) of eight random bases was used to label the pre-amplified cDNA, which eliminated the duplication bias in PCR and sequencing steps. 200–500 bps library products were enriched, quantified and sequenced on DNBSEQ-T7 sequencer (MGI Tech Co., Ltd. China).

Low-quality reads were discarded and the reads contaminated with adaptor sequences were trimmed in the raw sequencing data by Trimmomatic (version 0.36). To eliminate duplication bias, clean reads were firstly grouped to specific clusters according to UMI sequences. Reads in the same cluster were compared to each other by pairwise alignment, and then reads with sequence identity over 95% were extracted to a new sub-cluster. For each sub-cluster, multiple sequence alignment was performed to get one consensus sequence. After de-duplicating, standard RNA-seq analysis was performed. Fastq files were aligned to GRCm38 reference genome using STAR software (version 2.5.3a) with default parameters. Reads aligned to the exon regions were counted by featureCounts (Subread-1.5.1; Bioconductor).

2.19 | Protein Extraction

Sequencing specimens for EVs were isolated from NSCs culture media in a single batch. Each sample (approximately 50 mL per specimen) derived from culture supernatants of NSCs belonging to different experimental groups. HypoNSCs-EVs and normoNSCs-EVs were ground into fine powder in liquid nitrogen

20013078, 2025, 7, Downloaded from https://isevjournals.onlinelibrary.wiley.com/doi/10.1002/jev2.70126 by CochraneChina, Wiley Online Library on [27/07/2025]. See the Terms and Conditions (https://onlinelibrary.wiley.com/terms-and-conditions) on Wiley Online Library for rules of use; OA articles are governed by the applicable Creative Commons License

and homogenized in 1 mL phenol, 1 mL saturated phenol with Tris-HCl (pH 7.5) was then added and the mixture was kept at 4°C for 30 min and centrifuged at 7000 × *g* for 10 min. The upper phenolic phase was transferred to a fresh tube and mixed with five volumes of 0.1 M ammonium acetate-methanol and kept at −20°C overnight. The mixture was centrifuged at 12,000 × *g* for 10 min and the protein pellet was washed twice with pre-cold methanol and twice with ice-cold acetone. Subsequently, protein pellet was air-dried and resuspended with 300 μL lysate solution. After incubation of 3 h at room temperature, insoluble fractions were removed by centrifugation and the protein supernatants were quantified concentrations by bicinchoninic acid assay.

2.20 | Protein Digestion

Protein samples with equal amounts were diluted with DTT solution to make the DTT final concentration about 5 mM, and incubated at 55°C for 30–60 min. Iodoacetamide was then added with final concentration of 10 mM, and incubated at room temperature for 30 min in dark. Proteins were precipitated by adding six times of acetone and kept at −20°C overnight. After centrifugation of 8000 × *g* for 10 min, pellets were resuspended in trypsin-TPCK diluent (1 mg/mL) and incubated at 37°C overnight. After enzymolysis, samples were lyophilized and stored at −80°C.

2.21 | Protein Labelling

To label with TMT/iTRAQ, lyophilized peptide samples were suspended in 100 mM TEAB (Sigma–Aldrich). TMT/ITRAQ label reagents (diluted with acetonitrile) were then mixed with peptide samples and incubated at room temperature for 1 h. After terminating reaction by adding 5% hydroxylamine and incubating for 15 min, labelling peptides solutions were lyophilized and stored at −80°C.

2.22 | Liquid Chromatography-Mass Spectrometry

The Proteomic data were analysed by Shanghai Luming biological technology co., LTD (Shanghai, China). RP separation was performed on an 1100 HPLC System (Agilent) using an Agilent Zorbax Extend RP column (5 μm, 2.1 mm × 150 mm). Mobile phases A (2% acetonitrile in HPLC water, pH = 10) and B (90% acetonitrile in HPLC water, pH = 10) were used for RP gradient. The solvent gradient was set as follows: 0–8 min, 98% A; 8–8.01 min, 98%–95% A; 8.01–30 min, 95%–80% A; 30–43 min, 80%–65% A; 43–53 min, 65%–55% A; 53–53.01 min, 55%–10% A; 53.01–63 min, 10% A; 63–63.01 min, 10%–98%A; 63.01–68 min 98% A. Fluent flow rate was 300 μL/min and monitored wavelength was 210 nm. Samples were collected for 8–54 min, and eluent was collected in centrifugal tube 1–15 every minute in turn. Samples were recycled in this order until the end of gradient. The separated peptides were lyophilized and stored at −80°C for subsequent mass spectrometry detection.

All analyses were performed by a Q Exactive HF mass spectrometer (Thermo) equipped with a Nanospray Flex source (Thermo). Samples were separated by RP-C18 column (50 cm × 75 μm) on an EASY-nLCTM 1200 system (Thermo). The flow rate was 300 nL/min and linear gradient was 75 min (0–50 min, 2%–28% B; 50–60 min, 28%–42% B; 60–65 min, 42%–90%B; 65–75 min, 90% B. Mobile phase A = 0.1% FA in water and mobile phase B = 0.1% FA in ACN). Full MS scans were acquired in the mass range of 350–1500 m/z with a mass resolution of 45,000 and the AGC target value was set at 3e6. The 20 most intense peaks in MS were fragmented with higher-energy collisional dissociation (HCD) with collision energy of 32. MS/MS spectra were obtained with a resolution of 15,000 with an AGC target of 2e5 and a max injection time of 80 ms. The Q Exactive HF dynamic exclusion was set for 30.0 s and run under positive mode.

2.23 | Database Search

ProteomeDiscoverer 2.4.1.15 (Thermo) was used to search all of the raw data thoroughly based on uniprot-Mus musculus-10090-2023.2.1.fasta. Database search was performed with Trypsin digestion specificity. Alkylation on cysteine was considered as fixed modifications in the database searching. For protein quantification method, TMT/ITRAQ was selected. A global false discovery rate (FDR) was set to 0.01 and protein groups considered for quantification required at least one peptide.

2.24 | Differentially Expressing Genes and Proteins Identification

Identification of differentially expressed genes between groups of RNA-seq or proteomics data were performed using the R package limma (version 3.54.2). Gene sets of Gene ontology (GO) and Kyoto encyclopaedia of genes and genomes (KEGG) were collected from MSigDB website and enrichment analysis were performed by R package clusterProfiler (version 4.6.2). The global false discovery rate (FDR) was set to 0.01.

2.25 | Plasmid Construction and shRNA Transfection

pSLenti-U6-shRNA-CMV-EGFP-F2A-Puro-WPRE vector plasmid was constructed to specifically target Rab17 or Hif-1a. Negative Control of short hairpin RNA was used as the negative control (shNC). The sequence information of short heparin RNA (shRNA) targeting to Rab17 or Hif-1a was displayed in **Table S2**. shRNA plasmids were transfected into primary NSCs using Lipofectamine 3000 reagent (Invitrogen) following the manufacture's manual. The inhibition of expression was determined by Western blot at 48 h after transfection.

2.26 | Engineering EVs Construction and Characteristic

We synthesized DSPE-PEG2000 conjugates of the CAQK and Angiopep2 peptides for targeted modification. These conjugates, along with DSPE-PEG2000 and DSPE-PEG2000-FITC, were procured from ShanXi BeiOu Biological Technology Co., Ltd (Xi'an, China). The functional DSPE conjugates were then integrated into EVs using established modification protocols. (Liang et al. 2024). The stock solution was first prepared by dissolving the

20013078, 2025, 7, Downloaded from https://isevjournals.onlinelibrary.wiley.com/doi/10.1002/jev2.70126 by CochraneChina, Wiley Online Library on [27/07/2025]. See the Terms and Conditions (https://onlinelibrary.wiley.com/terms-and-conditions) on Wiley Online Library for rules of use; OA articles are governed by the applicable Creative Commons License

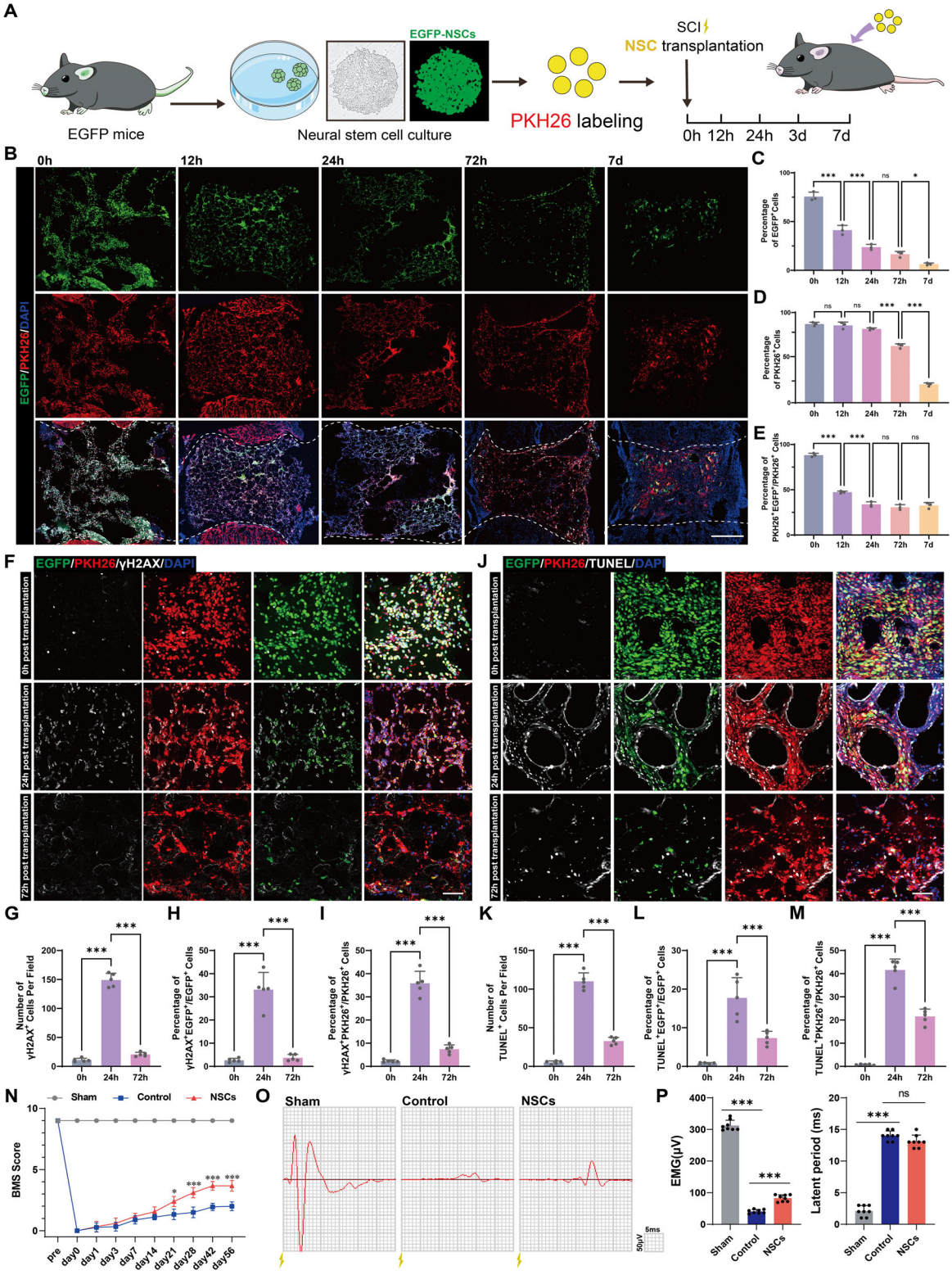

FIGURE 1 | Legend on next page.

DSPE functional conjugation in dimethyl sulfoxide (DMSO, Sigma–Aldrich, USA) at 500 μM; when in use, the working solution was prepared by dropwise addition to 1× PBS with continuous stirring for a final concentration of 5 μM. Meanwhile, 100 μg EV samples (containing 2.5×10^{11} particles) were diluted to 1 mL with PBS. Taking EVs: DSPE-PEG2000 anchor = 1:5000 as an example, a total 500 μL DSPE-PEG2000-anchor work solution was added dropwise to the EVs aqueous with continuous stirring at room temperature. This modification mixture was then incubated for 1 h at 37°C upon shaking to facilitate the hydrophobic insertion of functional conjugation into the EV membrane. Subsequently, non-inserted functional conjugation

20013078, 2025, 7, Downloaded from https://isevjournals.onlinelibrary.wiley.com/doi/10.1002/jev2.70126 by CochraneChina, Wiley Online Library on [27/07/2025]. See the Terms and Conditions (https://onlinelibrary.wiley.com/terms-and-conditions) on Wiley Online Library for rules of use; OA articles are governed by the applicable Creative Commons License

FIGURE 1 | **Transplanted NSCs are hypoxic and rarely differentiate into neurons**. (A) The Schematic of the transplanted NSCs tracing using EGFP-NSCs labelling with PKH26. (B) Representative immunofluorescent pictures showing survival of PKH26 labelled EGFP-NSCs (PKH26: Red; EGFP: Green) in spinal cord at 0, 12 h, 24 h, 72 h and 7d post-transplantation. Scale bar, 500 μm. (C) Quantification of EGFP positive cells the in (B). (D) Quantification of PKH26 positive cells the in (B). (E) Quantification of rate of EGFP and PKH26 double positive cells to PKH26 single positive cells in (B). $N = 5$ per group. (F) Representative immunofluorescent pictures showing PKH26 labelled EGFP-NSCs (PKH26: Red; EGFP: Green) co-labelling with γH2AX (White) in spinal cord at 0, 24 and 72 h post-transplantation. Scale bar, 100 μm. (G) Quantification of γH2AX positive cells the in epicentre of SCI mice 0, 24 and 72 h post transplantation in (F). $N = 5$ per group. (H) Quantification of percentage of $\gamma H2AX^+EGFP^+$ cells/$EGFP^+$ cells the in epicentre of SCI mice 0, 24 and 72 h post transplantation in (F) $N = 5$ per group. (I) Quantification of percentage of $\gamma H2AX^+PHK26^+$ cells/$PKH26^+$ cells the in epicentre of SCI mice 0, 24 and 72 h post transplantation in (F) $N = 5$ per group. (J) Representative immunofluorescent pictures showing PKH26 labelled EGFP-NSCs (PKH26: Red; EGFP: Green) co-labelling with TUNEL signaling (White) in spinal cord at 0, 24 and 72 h post-transplantation. Scale bar, 100 μm. (J) Quantification of TUNEL positive cells the in epicentre of SCI mice 0, 24 and 72 h post transplantation in (J). $N = 5$ per group. (L) Quantification of percentage of $TUNEL^+EGFP^+$ cells/ the $EGFP^+$ cells in epicentre of SCI mice 0, 24 and 72 h post transplantation in (J). $N = 5$ per group. (M) Quantification of percentage of $TUNEL^+PKH26^+$ cells/ the $PKH26^+$ cells in epicentre of SCI mice 0, 24 and 72 h post transplantation in (J). $N = 5$ per group. (N) BMS scores in sham, control, NSCs-treated groups at different time points post-SCI. $N = 10$ per group. * Control versus NSCs-treated groups. (O) Representative electrophysiological trace images were recorded in each group at 8 weeks post-SCI. (P) Measurement of the MEP amplitude and latent period in (O). $N = 8$ per group. Data are presented as mean ± SD, NS, no significant difference, $^*p < 0.05$, $^{**}p < 0.01$, $^{***}p < 0.001$.

molecules were separated via ultrafiltration by centrifugation on a 100 kDa centrifugal filter. The purification procedure after modification was the same as that after labelling. The final retentate was adjusted to ~0.5 μg/μL prior to subsequent use or freezing. The ratio of the two peptides used in the dual-modification was 1:1, the number of any peptide in the single modification was the same as that of the same peptide in the dual-modification, and the other peptide used in the dual-modification was replaced by the same number of DSPE-PEG2000. To confirm that DSPE-PEG2000 can be successfully inserted into the EVs, DSPE-PEG2000-FITC was added to the diluted EV solution as described above. Insertion of DSPE-PEG2000-FITC on the EV surface was confirmed by visualizing labelled EVs using flow cytometry. We carried out the process above using various molar ratios of DSPE-PEG2000-FITC to EV particles at 100:1, 500:1, 1000:1, 2000:1, 4000:1, 8000:1 and 16000:1, followed by purification by ultrafiltration.

2.27 | In Vivo Tracing of EVs Derived From Transplanted NSCs

The CD63-copGFP-Flag lentiviral vector system was engineered to leverage the vesicular membrane localization properties of CD63, theoretically enabling GFP signals to specifically label secreted EVs. To trace the EVs released from implemented NSCs in vivo, CD63-copGFP-Flag Lentifect (GeneCopoeia) was transfected into primary cultivated NSCs following the user's manual. Briefly, NSCs were dissociated and plated in 6-well plate at a density of 500,000 cells per dish 24 h prior to viral infection. Virus particles were diluted in NSC growth medium containing Polybrene (OBiO) at MOI = 20. NSCs were collected, centrifuged and resuspended in diluted viral medium. After incubation at 37°C for 12 h, NSCs were centrifuged and resuspended in fresh NSC growth medium (without Polybrene and virus), and continued to be cultivated at 37°C with 5% CO_2 for 3 days. Ultimately, fluorescence NSCs were counted and implemented into the injury site. Twenty-four hours post-transplantation, spinal cord tissues from CD63-GFP-NSC transplanted mice were cryosectioned for histological analysis. The cellular uptake of NSC-derived EVs by target cells was analysed using immunofluorescence labelling (CD11b/CD31/NeuN) combined with GFP signal colocalization tracking from CD63-tagged EVs.

2.28 | EVs Labelling and In Vivo Tracking

The EVs were resuspended in ultra-pure water to a protein concentration of 1.0 μg/μL. The resuspended EVs were then stained with PKH67 Red Fluorescent Cell Linker Kits for General Cell Membrane Labelling (Sigma–Aldrich) for immunostaining to monitor EV uptake and DiR Iodide (DiIC18(7)) Cell Membrane Fluorescent Probe (Yeason) for in vivo EV tracking. For labelling, the EV solution was incubated with 5 μg/mL PKH67 or DIR dye for 30 min. The unincorporated dyes were removed using 300-kDa ultrafiltration tubes (Pall Corp.) and washed in PBS with ultracentrifugation. To detect the in vivo image of the mice after EVs administration, a mixture of DiR or PKH67 fluorescent-labelled EVs were injected into the SCI mice through the tail vein. To mitigate false-positive signals during in vivo EV-tracking, EV suspensions were subjected to ultracentrifugation at 100,000 × *g* for 2 h, and the supernatant were harvest and undergoing the same dilution, incubation, and purification steps refer to the PKH67 labelling protocol (PKH67-labelled EV-free control) (Pužar Dominkuš et al. 2018; Takov et al. 2017). Twenty-four hours post-injury, the spinal cord tissue was harvested from the PKH67-EVs administrated mice and sectioned for immunostaining to analyse the uptake of EVs in the peripheral cells adjacent to the lesion site. The mice treated with DiR-labelled EVs were scarified at 24 h post-SCI. The spinal cord and visceral tissues were imaged using Xenogen IVIS Imaging System (Caliper Life Sciences).

2.29 | Locomotor Function and Neuroelectrophysiological Evaluation

The Basso Mouse Scale (BMS) score was independently assessed by two blinded observers, unaware of the experimental group assignments (Basso et al. 2006). For the transsectional SCI model, the evaluation time points are pre-injury, immediately post-injury, and 1, 3, 7, 14, 21, 28, 42 and 56 days post-injury (dpi). For the contusion SCI model, the evaluation time points are pre-injury, immediately post-injury, and 1, 3, 7, 14, 21, and 28 dpi. The procedure involved placing the mice in an open field for a 4-min period to assess their motor recovery post-SCI. The scoring system, ranging from 0 to 9, was based on various parameters of hind limb movement observed in the open field, including joint

20013078, 2025, 7, Downloaded from https://isevjournals.onlinelibrary.wiley.com/doi/10.1002/jev2.70126 by CochraneChina, Wiley Online Library on [27/07/2025]. See the Terms and Conditions (https://onlinelibrary.wiley.com/terms-and-conditions) on Wiley Online Library for rules of use; OA articles are governed by the applicable Creative Commons License

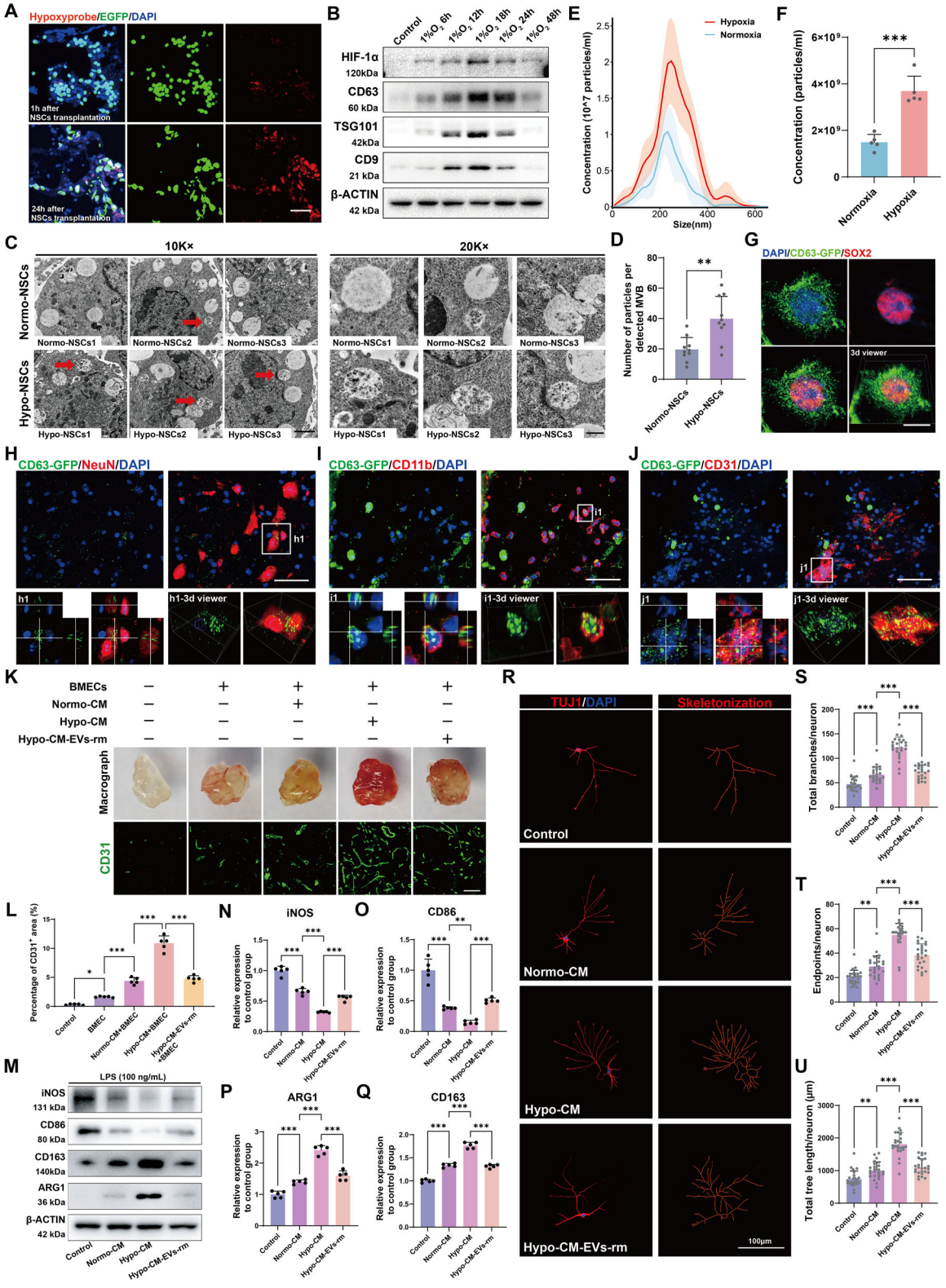

FIGURE 2 | Legend on next page.

mobility, weight-bearing capacity, foot placement, coordination, paw positioning, and control of the trunk and tail. A score of 0 denoted complete paralysis of the hind limbs, whereas a score of 9 signified normal locomotor function. For the documentation of motor-evoked potentials (MEPs), the mice were anesthetized with 0.3% Pentobarbital Sodium (70 mg/kg). After being shaved and disinfected, they were positioned in a stereotactic frame, and their body temperature was carefully regulated using a heating pad. A craniotomy was performed to expose the motor cortex, and a stimulation electrode was precisely guided to a depth of 700–1000 μm from the cortical surface using stereotactic guidance, targeting the corticospinal neurons within the sensorimotor cor-

20013078, 2025, 7, Downloaded from https://isevjournals.onlinelibrary.wiley.com/doi/10.1002/jev2.70126 by CochraneChina, Wiley Online Library on [27/07/2025]. See the Terms and Conditions (https://onlinelibrary.wiley.com/terms-and-conditions) on Wiley Online Library for rules of use; OA articles are governed by the applicable Creative Commons License

FIGURE 2 | Hypoxia-induced NSCs-EVs release could be taken up by neuron cells, endothelial cells, and microglia, facilitating a regenerative phenotype. (A) Representative immunofluorescent pictures showing EGFP-labelled NSCs (Green fluoresce) co-labelling with Hypoxyprobe (Red fluoresce) at 1 and 24 h post-transplantation. Scale bar, 50 μm. (B) Western blotting analysis of the expression of specific extracellular vesicle markers, including CD9, CD63 and TSG101, alongside the hypoxia-associated marker HIF-1α. (C) Transmission Electron Microscopy images of cultured NSCs under nomoxic or hypoxic condition in vitro (scale bar, 1 μm). The red arrows indicated the Multivesicular bodies (MVBs)—cavities wrapped by a double membrane containing 10–50 intracavitary vesicles with a medium electron density. (D) Particles per MVB detected in the nomoxic or hypoxic NSCs. Particles per MVB were quantified across 10 randomly selected microscopic fields ($N = 10$ fields analyzed). (E) Nanoparticle tracking analysis of the EVs from NSCs culture medium under normal or hypoxia condition. (F) Quantification of average EVs concentration in the NSCs culture medium under normal or hypoxia condition. $N = 5$ per group from five culture plate. (G) Identification of CD63-copGFP-Flag Lentifect transfected nomoxic NSC in vitro using immunofluorescent detection co-labelling with specific stem cell marker SOX2 at single cell level, scale bar, 10 μm. The bottom-right image representing a 3D viewer of the immunofluorescent picture. (H) Representative immunofluorescent pictures showing CD63-GFP-labelled NSCs-EVs (Green) co-labelling with NeuN (Red) at 24 h post-transplantation. Scale bar, 50 μm. (h1-left) Magnified white square region (as indicated). (h1-right) 3D viewer of white square region (as indicated). (I) Representative immunofluorescent pictures showing CD63-GFP-labelled NSCs-EVs (Green) co-labelling with CD11b (Red) at 24 h post-transplantation. Scale bar, 50 μm. (i1-left) Magnified white square region (as indicated). (i1-right) 3D viewer of white square region (as indicated). (J) Representative immunofluorescent pictures showing CD63-copGFP-labelled NSCs-EVs (Green) co-labelling with CD31 (Red) at 24 h post-transplantation. Scale bar, 50 μm. (j1-left) Magnified white square region (as indicated). (j1-right) 3D viewer of white square region (as indicated). (K) Photographic presentation and the immunofluorescent section of the isolated gels for in vivo angiogenesis. Scale bar, 100 μm. (L) Quantification of CD31 positive signals in the isolated gels for in vivo angiogenesis of the control, BMECs, BMECs + Normo-CM, BMECs + Hypo-CM, and BMECs + Hypo-CM-EVs-rm groups in (K). $N = 5$ per group. (M) Western blot analysis of the inflammatory markers of iNOS, CD86 and the anti-inflammation markers of CD163, ARG1 of the control, BMECs, BMECs + Normo-CM, BMECs + Hypo-CM, and BMECs + Hypo-CM-EVs-rm groups under LPS treatment (100 ng/mL). The control group refers to the BV2 cells treated with equal volume of NSC conditional medium (without cell culture). (N-Q) Quantification of iNOS, CD86, CD163 and ARG1 expression in (M). $N = 5$ per group. (R) Representative immunofluorescent stains of anti-TUJ1 images of cultured neurons after NSCs-CM administration. The control group refers to the neural cells treated with fresh culture medium that has not been used to cultivate NSCs. (S-U) Quantification of branches /neuron, endpoints/neuron and the total tree length in (R). $N = 25$ per group (Five random fields of view were chosen from five independent plates for quantification). Data are presented as mean ± SD, NS, no significant difference, $^{*}p < 0.05$, $^{**}p < 0.01$, $^{***}p < 0.001$.

tex. The recording electrode was strategically placed at the distal end of the contralateral thigh's sciatic nerve to detect the muscle action potential elicited by electrical stimulation. The Cereplex direct system (Blackrock) was employed for the amplification and recording of the bioelectrical signals. The stimulation parameters were meticulously chosen to include fine voltage control, single pulse mode, a 100 ms inter-stimulus interval, a frequency of 100 Hz, and an applied voltage of 14 V.

2.30 | Statistical Analysis

Results are represented as mean values ± SD, and n values represent the number of animals in the experiments. Statistical analysis was carried out using Prism 8 software. Differences were considered statistically significant at values listed as follows: $^{*}p < 0.05$, $^{**}p < 0.01$, and $^{***}p < 0.001$. Statistical comparisons of two groups were conducted using a two-tailed unpaired Student's t-test. Differences among multiple groups were analysed with one-way ANOVA followed by Tukey's post hoc tests. The analysis of BMS scores were analysed with repeated-measures two-way ANOVA at different time points.

3 | Results

3.1 | Despite Apoptosis and Limited Differentiation, NSC-Transplantation Still Aids SCI Repair

To delineate the therapeutic impact of NSC transplantation on SCI repair, we sourced NSCs from the spinal cords of postnatal mice, validated by positive NESTIN and SOX2 immunostaining (Figure S1A,B). The green fluorescent-labelled NSCs ($EGFP^{+}$NSCs) were extracted from the EGFP mice (the whole-body cells expressed green fluorescent protein) and embedded within the SCI site and integrated with a matrix gel to investigate the survival and differentiation of transplanted NSCs in vivo. Upon examination, 2 months post-transplantation of NSCs, it was observed that the majority of $EGFP^{+}$ NSCs exhibited co-staining with GFAP, while virtually no co-staining with NeuN was detected (Figure S2A), suggesting that the majority of transplanted NSCs predominantly differentiate into astrocytes, with minimal neuronal differentiation. Employing flow cytometry and immunofluorescent staining techniques, a significant reduction in the NSC population was noted over time, culminating in approximately 99% loss by 7 days post-injection (Figure S3A,B). Using histological detection to detect the survival of transplanted NSCs in vivo, a dual-labelling strategy (EGFP/PKH26) to address fluorescence protein expression variability, wherein PKH26 and EGFP co-localization serves as a viability benchmark while PKH26 monostaining identifies apoptotic or dysfunctional cells (Figure 1A). Histological analysis revealed a >60% attenuation of EGFP fluorescence in transplanted NSCs within 24 h post-injury, indicative of cell death or viability loss. In contrast, PKH26-labelled NSCs exhibited stable membrane localization without significant signal reduction during this acute phase (<24 h), confirming its reliability for tracking spatial distribution of transplanted cells regardless of viability status (Figure 1B–E). Leveraging this dual-labelling strategy, immunofluorescence further demonstrated DNA damage signatures (Phosphorylated histone H2AX, γH2AX) in transplanted NSCs. Co-labelling of γH2AX with EGFP/PKH26 demonstrated elevation of γH2AX expression in transplanted NSCs within 24 h, synchronized with the decline of $EGFP^{+}$ NSCs, indicating temporally correlated acti-

20013078, 2025, 7, Downloaded from https://isevjournals.onlinelibrary.wiley.com/doi/10.1002/jev2.70126 by CochraneChina, Wiley Online Library on [27/07/2025]. See the Terms and Conditions (https://onlinelibrary.wiley.com/terms-and-conditions) on Wiley Online Library for rules of use; OA articles are governed by the applicable Creative Commons License

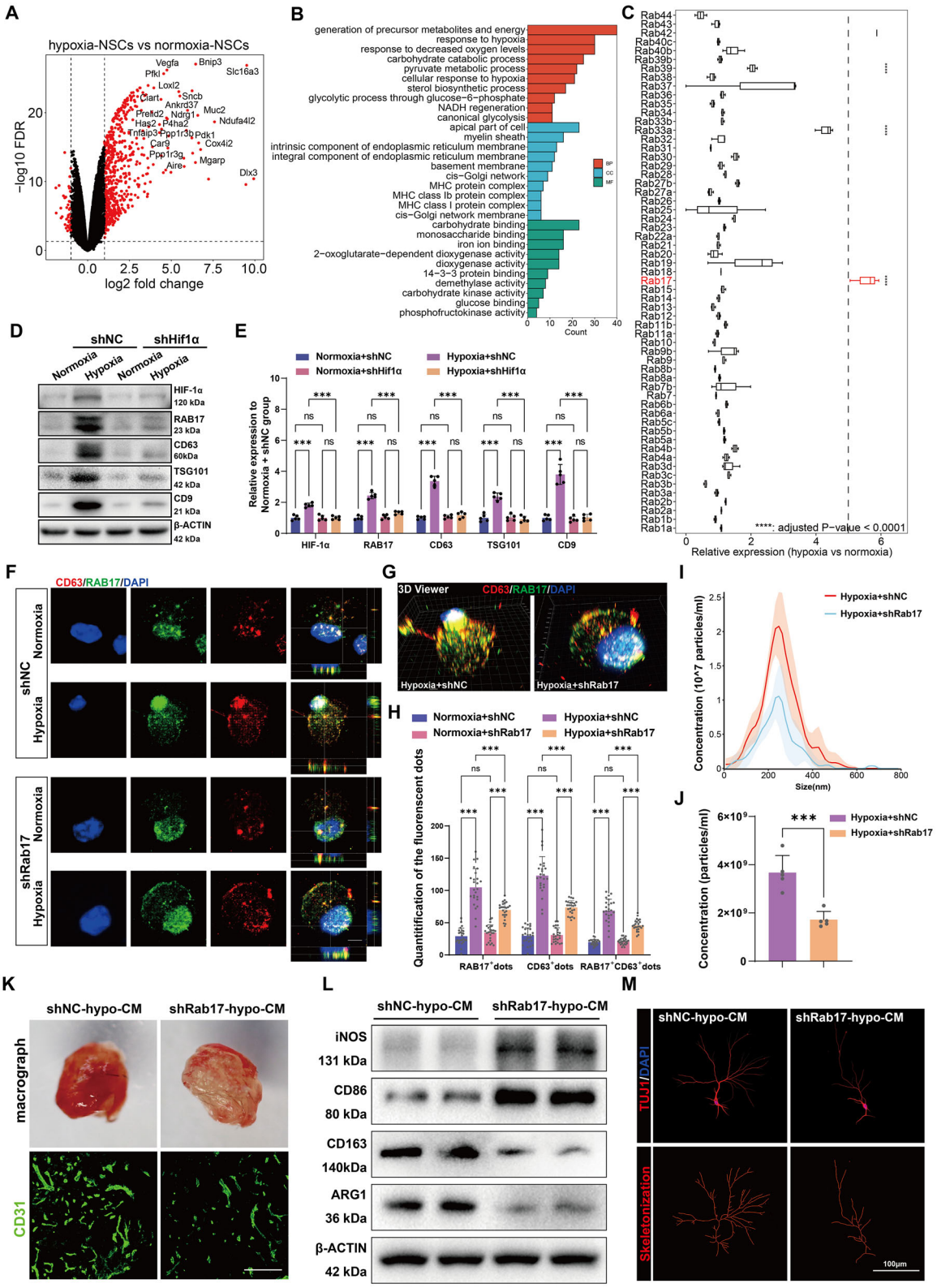

FIGURE 3 | Legend on next page.

vation of DNA damage response alongside cell loss (Figure 1F–I). Furthermore, it was noted that within 24 h after transplantation, there was a significant decrease in EGFP$^+$NSCs, accompanied by an increase in apoptotic frequency (Figure 1J–M). However, despite apoptosis and limited differentiation, over 8 weeks post-SCI, the mice treated with NSC-transplantation exhibited superior hindlimb motor recovery, as evidenced by Basso Mouse Scale (BMS) (Figures 1N and S4A). Electrophysiological assessments revealed a statistically significant enhancement in lower limb motor evoked potential (MEP) amplitude in the NSCs-

20013078, 2025, 7, Downloaded from https://isevjournals.onlinelibrary.wiley.com/doi/10.1002/jev2.70126 by CochraneChina, Wiley Online Library on [27/07/2025]. See the Terms and Conditions (https://onlinelibrary.wiley.com/terms-and-conditions) on Wiley Online Library for rules of use; OA articles are governed by the applicable Creative Commons License

FIGURE 3 | Hypoxia induced HIF-1α/Rab17 upregulation facilitated the regenerative phenotype. (A) Volcano plot shows the mRNA expression pattern of the hypoxia NSCs. (B) GO pathway analysis of the upregulated mRNA expression pattern of the hypoxia NSCs. (C) The expression pattern of the RAB family in the hypoxia NSCs. (D) Western blot analysis of the HIF-1α and the EVs relative markers including CD63, CD9, TSG101 and RAB17. (E) Quantification of HIF-1α and RAB17 expression in (D). $N = 5$ per group. (F) Stimulated emission depletion (STED) super-resolution imaging of CD63 and RAB17 immunofluorescent stains of cultured NSCs after RAB17 knockdown and hypoxia administration. Scale bar, 2 μm. (G) 3D vision of the imaging of CD63 and RAB17 immunofluorescent stains of the cultured NSCs. (H) Quantification RAB17 and CD63 expression in (F). $N = 25$ per group. (I) Nanoparticle tracking analysis of the EVs from NSCs culture medium of the shNC and shRab17 treated NSCs under hypoxia condition. (J) Quantification of average EVs concentration in the NSCs culture medium under hypoxia condition of the shNC and shRab17 groups. $N = 5$ per group from five culture plate. (K) Photographic presentation and the immunofluorescent section of the isolated gels mixed with hypoxic CM isolated from shNC or shRab17 treated NSCs (shNC-hypo-CM vs shRab17-hypo-CM) for in vivo angiogenesis. Scale bar, 100 μm. (L) Western blot analysis of the inflammatory markers of iNOS, CD86 and the anti-inflammation markers of CD163, ARG1 in BV2 cells of the shNC-hypo-CM and shRab17-hypo-CM treated groups. (M) Representative immunofluorescent stains of anti-TUJ1 images of cultured neurons after shRab17-hypo-CM or shNC-hypo-CM administration. Scale bar, 100 μm. Data are presented as mean ± SD, NS, no significant difference, $^{*}p < 0.05$, $^{**}p < 0.01$, $^{***}p < 0.001$.

treated cohort at 56 days post-injury (dpi), notwithstanding the persistent latency period (Figure 1O-P). Histologically, NSCs group displayed enhanced spinal cord coherence without atrophy (Figure S4B). Immunofluorescence for CSPG and laminin showed that NSC transplantation promoted glial scar contraction and reduced lesion size, partially restoring spinal cord continuity (Figure S5A,E,F). Reduced CD68 staining suggested decreased inflammation post-NSC transplantation (Figure S5B,G). CD31 staining for vascular morphology detection indicated less vascular remodelling with reduced diameter in the NSCs-treated group (Figure S5C,H,I). Employing immunofluorescence to identify neural fibres at the injury site, NSCs transplantation substantially enhanced nerve ingrowth following SCI (Figures S5D and S3J). The findings highlight that the local environment after NSCs transplantation poses challenges to cell survival and differentiation, necessitating further investigation into the mechanisms of NSC-transplantation in SCI repair.

3.2 | Hypoxia-Induced NSCs-EVs Release Could be Taken Up by Neuron Cells, Endothelial Cells, and Microglia, Facilitating a Regenerative Phenotype

To elucidate the mechanisms by which transplanted NSCs enhance SCI repair, we utilized a hypoxia probe to detect cellular responses, revealing that the majority of surviving NSCs exhibited hypoxic conditions 24 h post-transplantation (Figure 2A). Adaptation to hypoxic environments can lead to metabolic and signalling pathway alterations, potentially influencing the secretion profile of EVs (Wang et al. 2014). Employing an in vitro hypoxia induction model at 1% O_2, we observed that short-term (less than 18 h) hypoxia did not compromise NSC viability or proliferation (Figure S6A,B). Western blot analysis indicated that HIF-1a expression increased with hypoxia duration, peaking at 18 h, correlating with the release of EVs-associated proteins such as CD63, CD9 and TSG101 (Figure 2B). Transmission electron microscopy of hypoxia-treated (1% O_2, 18 h) NSCs disclosed more multivesicular bodies (MVBs) structures and more vesicle particle in MVBs (Figure 2C,D). The nanoparticle tracking analysis (NTA) also confirmed heightened release of nanoscale particles under hypoxic conditions (Figure 2E,F). Further experiments involved transfection of NSCs with a EVs tracing virus (CD63-copGFP-Flag Lentifect) (Mathieu et al. 2021) (Figures 2G and S7A), followed by transplantation into SCI mice. CD63-GFP^{+} EVs originating from transplanted NSCs were spatially localized in peri-lesional regions, with internalization observed in multiple cell populations including neurons, microglia, and endothelial cells. This cellular uptake pattern was cross-validated through multi-scale fluorescence imaging (whole-tissue overview) and super-resolution microscopy, confirming EV delivery to recipient cells in the injured microenvironment (Figures 2H–J and S8A-C). Next, we utilized ultracentrifugation to remove EVs from the culture medium of hypoxia-induced NSCs (hypo-CM-EVs-rm). Through in vivo angiogenesis assay, microglial polarization models and neurite outgrowth assay, we further elucidated the role of hypoxia-induced NSCs in SCI repair. The depletion of EVs abrogated the pro-angiogenic effects of hypo-CM (Figure 2K–L). Western blot analysis revealed that hypo-CM induced an anti-inflammatory microglial phenotype after LPS (Lipopolysaccharide) treatment (Figure S9A,B), characterized by downregulated expression of pro-inflammatory markers (iNOS and CD86) and upregulated expression of anti-inflammatory markers (CD163 and ARG1) (Ransohoff 2016; Najem et al. 2024; Lan et al. 2017), and this phenomenon could be abolished upon EV removal (Figure 2M–Q). Morphometric analysis of neuronal skeletons revealed that hypo-CM treatment enhanced neurite complexity, which was attenuated upon EVs depletion (Figure 2R–U). Collectively, these findings highlight the pivotal role of hypoxia in modulating EVs secretion by NSCs and underscore the potential of these EVs in facilitating SCI regenerative phenotype.

3.3 | Hypoxia Induced HIF-1α/Rab17 Upregulation Facilitated the Regenerative Phenotype

To investigate the underlying mechanism of hypoxia-induced NSCs releasing EVs, the NSCs were cultured under normoxic and hypoxic conditions for RNA-seq sequencing. We obtained 1532 upregulated genes and 512 downregulated genes (Figure 3A). Further analysis of the upregulated genes after hypoxia treatment using GO pathway analysis revealed a significant increase in the expression of pathways related to hypoxia response and EVs release (Figure 3B). KEGG pathway analysis revealed that hypoxic treatment significantly upregulated the expression of multiple genes associated with the HIF-1α signalling pathway, including PDK1, FLT1, PFKL and other related factors (Figure S10A). The Rab family is closely associated with EV release (Wilmes and Kümmel 2023). By screening all Rab family genes, it was found that Rab17 showed the most significant upregulation after hypoxia treatment, exceeding five-fold (Figure 3C). To investigate the regulatory roles of Hif-1α and Rab17 in NSCs-EVs release, the sh-RNA for Hif-1α knocking-down were constructed, and trans-

20013078, 2025, 7, Downloaded from https://isevjournals.onlinelibrary.wiley.com/doi/10.1002/jev2.70126 by CochraneChina, Wiley Online Library on [27/07/2025]. See the Terms and Conditions (https://onlinelibrary.wiley.com/terms-and-conditions) on Wiley Online Library for rules of use; OA articles are governed by the applicable Creative Commons License

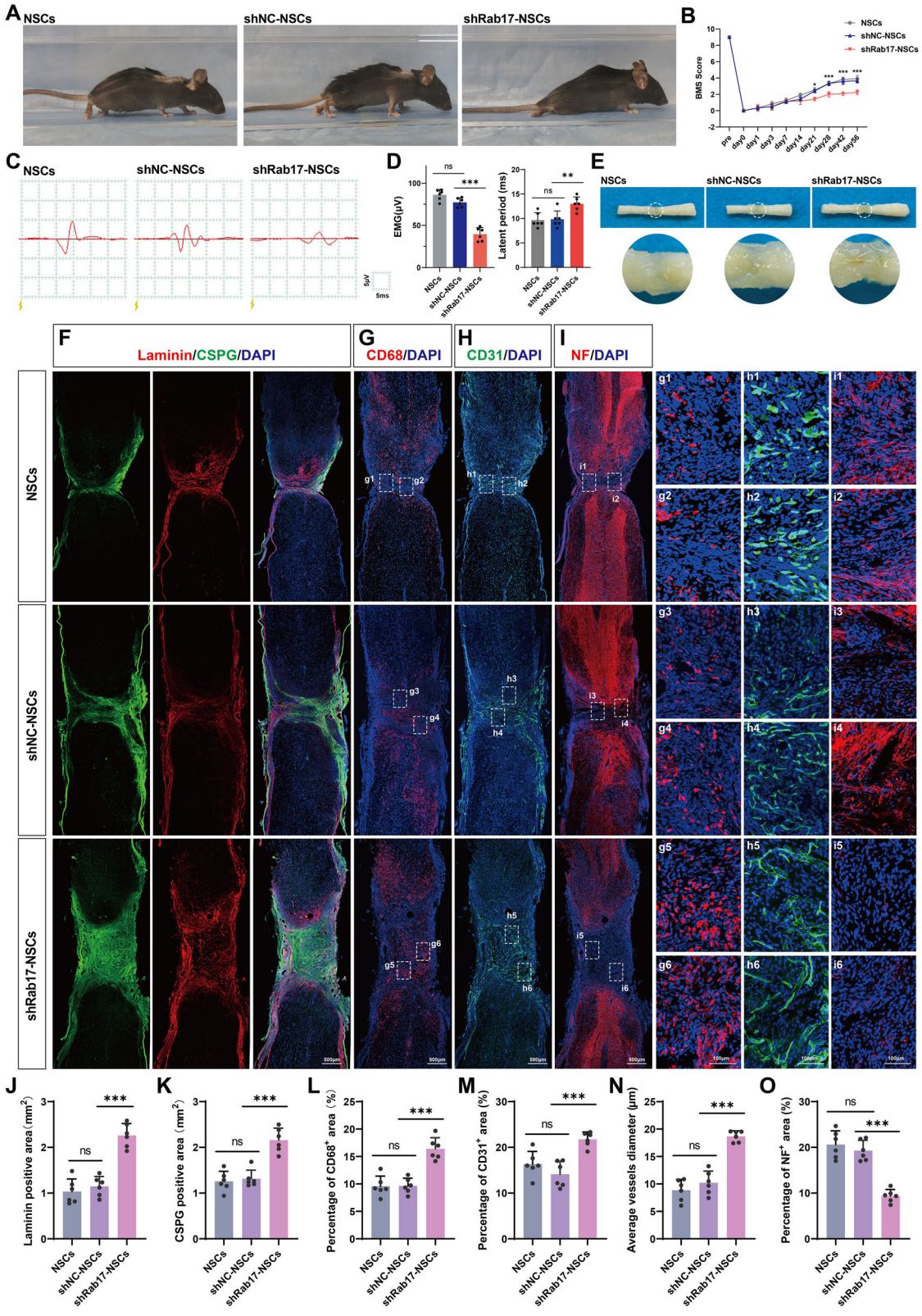

FIGURE 4 | Legend on next page.

fected into NSCs. Using WB analysis, we found that the expression of EVs-related marker proteins significantly decreased after knocking down Hif-1α, indicating that HIF-1α/RAB17 axis could regulate NSCs-EVs release (Figure 3D–E). To understand the role of Rab17 in regulate the EVs release, we also constructed the Rab17 sh-RNA. Under hypoxic condition, the knockdown efficiency of the shRab17-2# construct was the strongest, exceeding 50% compared to the shNC group. Therefore, we selected shRab17-2# for further experiments (Figure S11A,B). The WB analysis showed that the partial knocking-down of Rab17 did not affect

20013078, 2025, 7, Downloaded from https://isevjournals.onlinelibrary.wiley.com/doi/10.1002/jev2.70126 by CochraneChina, Wiley Online Library on [27/07/2025]. See the Terms and Conditions (https://onlinelibrary.wiley.com/terms-and-conditions) on Wiley Online Library for rules of use; OA articles are governed by the applicable Creative Commons License

FIGURE 4 | Rab17 knockout diminished the neuroregenerative potential of NSCs-transplantation, reducing its efficacy in SCI repair. (A) Representative pictures are showing hindlimb movement of mice at 8 weeks after spinal cord complete transection of the NSCs, shNC-NSCs and shRab17-NSCs treated groups. (B) BMS scores in NSCs, shNC-NSCs and shRab17-NSCs treated groups at different time points post-SCI. $N = 6$ per group. * NSCs versus shRab17-NSCs-treated groups. (C) Representative electrophysiological trace images were recorded in each group at 8 weeks post-SCI. (D) Measurement of the MEP amplitude and latent period in (C). (E) Photographic presentation of the isolated spinal cord in NSCs, shNC-NSCs and Rab17-NSCs treated groups. (F) Representative immunofluorescent stains of the scar tissue (CSPG, green, Laminin, Red) images of the spinal cord at 8 weeks post-injury in each group. Scale bar, 500 μm. (G) Representative immunofluorescent stains of CD68 (Red) images of the spinal cord at 8 weeks post-injury in each group. Scale bar, 500 μm. (g1-g6) Higher magnification of inflammatory cells in dotted boxes as indicated in (G). Scale bar: 100 μm. (H) Representative immunofluorescent stains of CD31 (Green) images of the spinal cord at 8 weeks post-injury in each group. Scale bar, 500 μm. (h1–h6) Higher magnification of remodelling vessels in dotted boxes as indicated in (I). Scale bar: 100 μm. (I) Representative immunofluorescent stains of Neurofilament (NF, Red) images of the spinal cord at 8 weeks post-injury in each group. Scale bar, 500 μm. (i1-i6) Higher magnification of regenerative neural fibres in dotted boxes as indicated in (I). Scale bar: 100 μm. (J) Quantification of CSPG positive signals in the epicentre of sham, control, NSCs-treated groups mice in (F). (K) Quantification of Laminin positive signals in the epicentre of NSCs, shNC-NSCs and Rab17-NSCs treated groups mice in (F). (L) Quantification of CD68 positive signals the epicentre of in NSCs, shNC-NSCs and Rab17-NSCs treated groups mice in (G). (M) Quantification of CD31 positive signals in the epicentre of NSCs, shNC-NSCs and Rab17-NSCs treated groups mice in (H). (N) Average vessels diameter quantification of CD31 positive vascular in the epicentre of in NSCs, shNC-NSCs and Rab17-NSCs treated groups mice in (H). (O) Quantification of NF positive signals in the epicentre of NSCs, shNC-NSCs and Rab17-NSCs treated groups mice in (I). Data are presented as mean ± SD, NS, no significant difference, $^{*}p < 0.05$, $^{**}p < 0.01$, $^{***}p < 0.001$.

HIF-1α activation, suggested that the knockdown of Rab17 does not affect the hypoxic stress of NSCs (Figure S11C,D). Using the 3D-stimulated Emission Depletion (3D-τ-STED) super-resolution imaging system, the immunofluorescence co-localization quantitative analysis shows that the EV marker CD63 and Rab17 present a significant spatial co-localization feature at the submicron resolution. Notably, knockdown of Rab17 not only significantly reduces the fluorescence signal intensity of CD63 but also decreases the number of co-localized fluorescence dots of CD63 and Rab17, suggesting that Rab17 may participate in the molecular interaction network of vesicle transport by regulating the anchoring effect of EV surface proteins (Figure 3F–H). NTA analysis also confirmed a significant decrease in the quantity of EVs formation after Rab17 knocking down (Figure 3I,J). Furthermore, the in vitro studies of the regenerative phenotype of hypo-CM after Rab17 knockout revealed that knocking out Rab17 significantly inhibited the promoting effects of hypo-CM on angiogenesis (Figures 3K and S12A), anti-inflammatory (Figures 3L and S12E-H), and neural growth (Figures 3M and S12B-C). These results preliminarily confirm that the HIF-1α/RAB17 axis is a key factor in hypoxia-induced NSCs releasing EVs.

3.4 | Rab17 Knockdown Attenuated the Neuroregenerative Promotion of NSCs Transplantation in SCI Repair

The Rab17-knockdown (KD) NSCs were engineered with a EVs marker virus (CD63-copGFP-Flag Lentifect) and subsequently transplanted into SCI mice. Post-SCI, the Rab17-KD NSCs treated mice exhibited a significantly attenuated accumulation of CD63-GFP^{+} EVs in the injured spinal cord, with minimal uptake by neural cells, endothelial cells, and microglia (Figure S13A–C), indicating that Rab17 knockout substantially reduced EVs release from NSCs post-transplantation. We then comprehensively assessed the consequences of this diminished EVs release on SCI repair. Over 3 weeks post-SCI induction, the hindlimb motor function recovery in the Rab17-KD NSCs treated group was compromised, as evidenced by BMS scores (Figure 4A,B). Electrophysiological testing revealed a significant reduction in lower limb MEP amplitude and prolonged latency at 56 dpi (Figure 4C,D). The spinal cord specimens from the shRab17-NSCs group displayed significant disruption in continuity and integrity (Figure 4E). Immunofluorescence analysis of the injured spinal cord indicated that Rab17 knockdown in NSCs transplantation exacerbated glial scar proliferation and increased the lesion area (Figure 4F,J,K). CD68 staining suggested heightened inflammation due to Rab17 knockdown in NSCs (Figure 4G,L). CD31 immunofluorescent staining indicated vascular remodelling induced by Rab17 knockdown (Figure 4H,M,N). Furthermore, immunofluorescence to label neural fibres at the injury site showed that Rab17 knockdown in transplanted NSCs significantly hindered nerve ingrowth post-SCI (Figure 4I,O). These findings collectively indicate that Rab17 knockout impaired the neuroregenerative potential of NSC transplantation in SCI repair.

3.5 | HypoNSCs-EVs Could Facilitate a Regenerative Phenotype in Endothelial Cells, Microglia and Neural Cells

Subsequently, we employed ultracentrifugation to isolate EVs from both normoxic NSCs and hypoxic NSCs (NormoNSCs-EVs and hypoNSCs-EVs) (Figure 5A). Protein mass spectrometry analysis was conducted on the EVs to delineate the proteomic profiles (Figure 5B). Among these upregulated proteins, a significant number of components have been identified as candidates for SCI repair. For instance, proteins such as Ccndl, Adnp and Hsp90aa1 exhibit significant neural regenerative potential, while Vegfa, Pdcl3 and Hsp90ab1 are associated with promoting angiogenesis (Hu et al. 2024; Hagey et al. 2020; Gozes et al. 2015; Sun et al. 2020; Sin et al. 2019). Additionally, proteins like Atf7ip play a role in anti-inflammatory processes (Sin et al. 2019) (Figure 5C). The protein-protein interaction network analysis was performed on the upregulated proteins within the EVs to uncover enriched functionalities, indicating that proteins upregulated in hypoNSCs-EVs were associated with protein folding and stability, neuronal apoptosis inhibition, axonal growth promotion, VEGFR pathway activation. These results all suggest that the hypoNSCs-EVs contain a variety of bioactive substances that can play a potential role in promoting SCI repair from multiple aspects (Figure 5D). In vitro studies on endothelial cells, microglia, and

20013078, 2025, 7, Downloaded from https://isevjournals.onlinelibrary.wiley.com/doi/10.1002/jev2.70126 by CochraneChina, Wiley Online Library on [27/07/2025]. See the Terms and Conditions (https://onlinelibrary.wiley.com/terms-and-conditions) on Wiley Online Library for rules of use; OA articles are governed by the applicable Creative Commons License

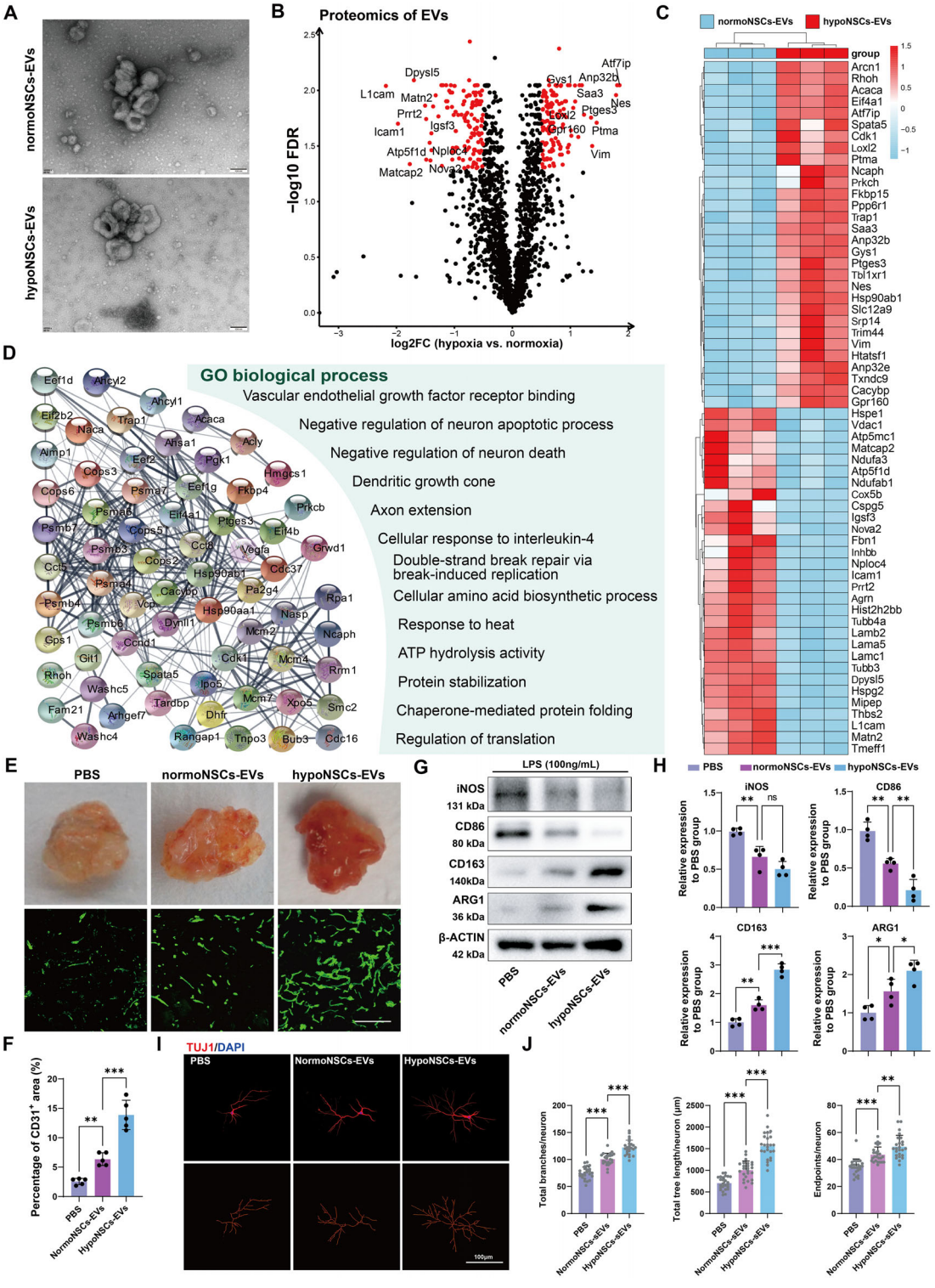

FIGURE 5 | Legend on next page.

neural cells treated with hypoNSCs-EVs demonstrated that these vesicles could foster angiogenesis (Figure 5E,F), induce anti-inflammatory phenotype in microglial cells (Figure 5G,H), and stimulate neural growth (Figure 5I,J). Collectively, these findings suggest that hypoNSCs-EVs contain a multitude of essential biochemical factors that promote regenerative phenotypes following SCI.

3.6 | Angiopep2 and CAQK Double-Labelled EVs Exhibited Improved Targeting Specificity to the Injury Area, Internalizing by Cells Within the Injury Site

Our initial findings have established that hypoNSCs-EVs have a compelling capacity to induce a regenerative phenotype. To augment the targeting precision and clinical viability of these

20013078, 2025, 7, Downloaded from https://isevjournals.onlinelibrary.wiley.com/doi/10.1002/jev2.70126 by CochraneChina, Wiley Online Library on [27/07/2025]. See the Terms and Conditions (https://onlinelibrary.wiley.com/terms-and-conditions) on Wiley Online Library for rules of use; OA articles are governed by the applicable Creative Commons License

FIGURE 5 | hypo-NSCs-EVs could facilitate a regenerative phenotype in endothelial cells, microglia and neural cells. (A) TEM image of EVs secreted by hypoxic NSCs and normoxic NSCs, scale bar, 100 nm. (B) Volcano plot shows the protein expression profile of the EVs isolated from the hypo-NSCs-CM. (C) Heatmap of the protein expression profile. (D) protein-protein interaction network analysis on the upregulated proteins in the hypoNSCs-EVs. (E) Photographic presentation and the immunofluorescent section of the isolated gels of the PBS, NormoNSCs-EVs and HypoNSCs-EVs groups for in vivo angiogenesis. Scale bar, 100 μm. (F) Quantification of CD31 positive signals in the isolated gels for in vivo angiogenesis of the PBS, NormoNSCs-EVs and HypoNSCs-EVs groups in (E), $N = 5$ per group. (G) Western blot analysis of the inflammatory markers of iNOS, CD86 and the anti-inflammation markers of CD163, ARG1 in LPS treated BV2 cells of the PBS, NormoNSCs-EVs and HypoNSCs-EVs groups. (H) Quantification of iNOS, CD86, CD163, and ARG1 expression in (G). $N = 5$ per group. (I) Representative immunofluorescent stains of anti-Tuj1 images of cultured neurons after PBS, NormoNSCs-EVs and HypoNSCs-EVs administration. Scale bar, 100 μm. (J) Quantification of branches /neuron, endpoints/neuron and the total tree length in (I). $N = 25$ per group (five random fields of view were chosen from five independent plates for quantification). Data are presented as mean ± SD, NS, no significant difference, $^{*}p < 0.05$, $^{**}p < 0.01$, $^{***}p < 0.001$.

vesicles, we conjugated them with the demyelinating area-targeting peptide CAQK and the blood–brain barrier-penetrating peptide Angiopep2 (Abi-Ghanem et al. 2022; Zhu et al. 2022; Habib and Singh 2022). As depicted in the schematic, in addition to the dual modification with DSPE-PEG2000-CAQK/DSPE-PEG2000-Angiopep2 (molar ratio 1:1), single modifications were performed using either one of the functional conjugates or the blank anchor DSPE-PEG2000 at an equivalent molar ratio, with EVs modified solely with blank anchor DSPE-PEG2000 serving as the control (Figure 6A). And the DSPE-PEG2000-mediated modification was validated using flow cytometry with DSPE-PEG2000-FITC to evaluate the binding efficiency to EVs. We found that at a mixing ratio of 8000 DSPE-PEG2000-FITC per EV particle, nearly 90% of EV particles were labelled with DSPE-PEG2000-FITC and showed FITC-positive signalling (Figure 6B,**C**). Base on the mixing ratio, this modification did not alter the size distribution of EVs, as both DSPE-PEG-modified and DSPE-PEG2000-CAQK/DSPE-PEG2000-Angiopep2 modified EVs maintained similar dimensions (Figure S14A,B). To assess the targeting efficacy of CAQK-Angiopep2-EVs to injured spinal cord tissue, DiR-labelled EVs, encompassing CAQK-EVs, Angiopep2-EVs, CAQK-Angiopep2-EVs, DSPE-PEG2000-EVs and native-EVs, were intravenously administered to mice with contusion SCI at a dose of 100 μg (~2.5 × 10^11 vesicles). To tracking the EVs within the spinal cord post injection, the animals were sacrificed 24 h post EV injection, and the spinal cord along with other major organs including brain, heart, lungs, liver, spleen, and kidneys were harvested and visualized using IVIS imaging. Notably, the CAQK-Angiopep2-EVs group displayed the most intense DiR signals in the injured spinal cord (Figure 6D–F). To view the distribution of CAQK-Angiopep2-EVs in the injured spinal cord, PKH67-labelled vesicles were injected to the contusion SCI mice. To eliminate interference from free proteins and PKH67 dye aggregates in the EV solution, a PKH67-labelled EV-free control was employed (Figure S15A–C). Considering that following contusion SCI, most neurons in the central injury area undergo apoptosis and may be lost entirely. The cellular uptake of EVs was analysed through spatially stratified histological assessment. Specifically, vascular endothelial cells and microglial EV internalization patterns were characterized within the lesion epicentre, while neuronal uptake dynamics were evaluated in the peri-lesional periphery (Figure 6G). Upon subsequent staining of spinal sections with cell-specific markers such as NeuN (neuronal marker), CD31 (endothelial cells), and CD11b (microglia), a distinct colocalization was observed between EVs and NeuN, CD11b, or CD31 in the epicentre and adjacent regions of the CAQK-Angiopep2-EVs group (Figure 6H–M). These results indicate that EVs dual-modified with CAQK and Angiopep2 demonstrate enhanced uptake by endothelial cells, neurons, and microglia in the epicentre and adjacent regions of SCI mice.

3.7 | CAQK and Angiopep2 Co-Modification EVs Significantly Promoted Functional Recovery Post SCI

To evaluate the potential biosafety of CAQK-Angiopep2, we administered HypoNSCs-EVs and CAQK-Angiopep2-HypoNSCs-EVs to 8-week-old naïve mice via intravenous injection (100 μg/d, 1 month). HE staining results confirmed that CAQK-Angiopep2-HypoNSCs-EVs did not induce cardiotoxicity, hepatotoxicity, spleen cell toxicity, pulmonary toxicity, or nephrotoxicity after 28-day intravenous injection of CAQK-Angiopep2-HypoNSCs-EVs, indicating favourable biosafety (Figure S16A–E). And utilizing the targeted drug delivery approach, we have conducted a comprehensive assessment of the therapeutic efficacy of EVs derived from various origins. This evaluation was carried out in a mouse model of SCI, which was established by creating a contusion injury. Subsequently, the therapeutic agents were administered via systemic injection of EVs into the tail vein of the mice. Over four consecutive weeks of evaluation after SCI induction, hindlimb motor function of the mice in the CAQK-Angiopep2-hypoNSCs-EVs treated group had better recovery regarding rear paw placement and hindlimb movement according to BMS scores (Figure 7A,B). The electrophysiological testing of the CAQK-Angiopep2-hypoNSCs-EVs treated mice demonstrated a significant increase in the amplitude of lower limb motor evoked potential (MEP) and reduced latency at 28 dpi (Figure 7C,D). Mice were sacrificed on day 28 after injury, and injured spinal cords were obtained and observed. As showing in Figure 7E, the spinal cord specimens from CAQK-Angiopep2-hypoNSCs-EVs group showed superior coherence and no obvious atrophy. Immunofluorescence analysis of the injured spinal cords indicated that CAQK-Angiopep2-hypoNSCs-EVs fostered glial scar contraction and diminished the lesion area (Figure 7F,J,K). CD68 staining, indicative of inflammatory activation, showed that CAQK-Angiopep2-hypoNSCs-EVs administration mitigated SCI-associated inflammation (Figure 7G,L). CD31 immunofluorescent staining suggested that CAQK-Angiopep2-hypoNSCs-EVs treatment reduced vascular remodelling (Figure 7H,M,N). Furthermore, immunofluorescence to delineate neural fibres at the injury site demonstrated that CAQK-Angiopep2-hypoNSCs-EVs significantly bolstered nerve ingrowth post-SCI (Figure 7I,O). Collectively, these findings suggest that hypoxia-induced NSCs-derived EVs offer significant benefits and potential in facilitating

20013078, 2025, 7, Downloaded from https://isevjournals.onlinelibrary.wiley.com/doi/10.1002/jev2.70126 by CochraneChina, Wiley Online Library on [27/07/2025]. See the Terms and Conditions (https://onlinelibrary.wiley.com/terms-and-conditions) on Wiley Online Library for rules of use; OA articles are governed by the applicable Creative Commons License

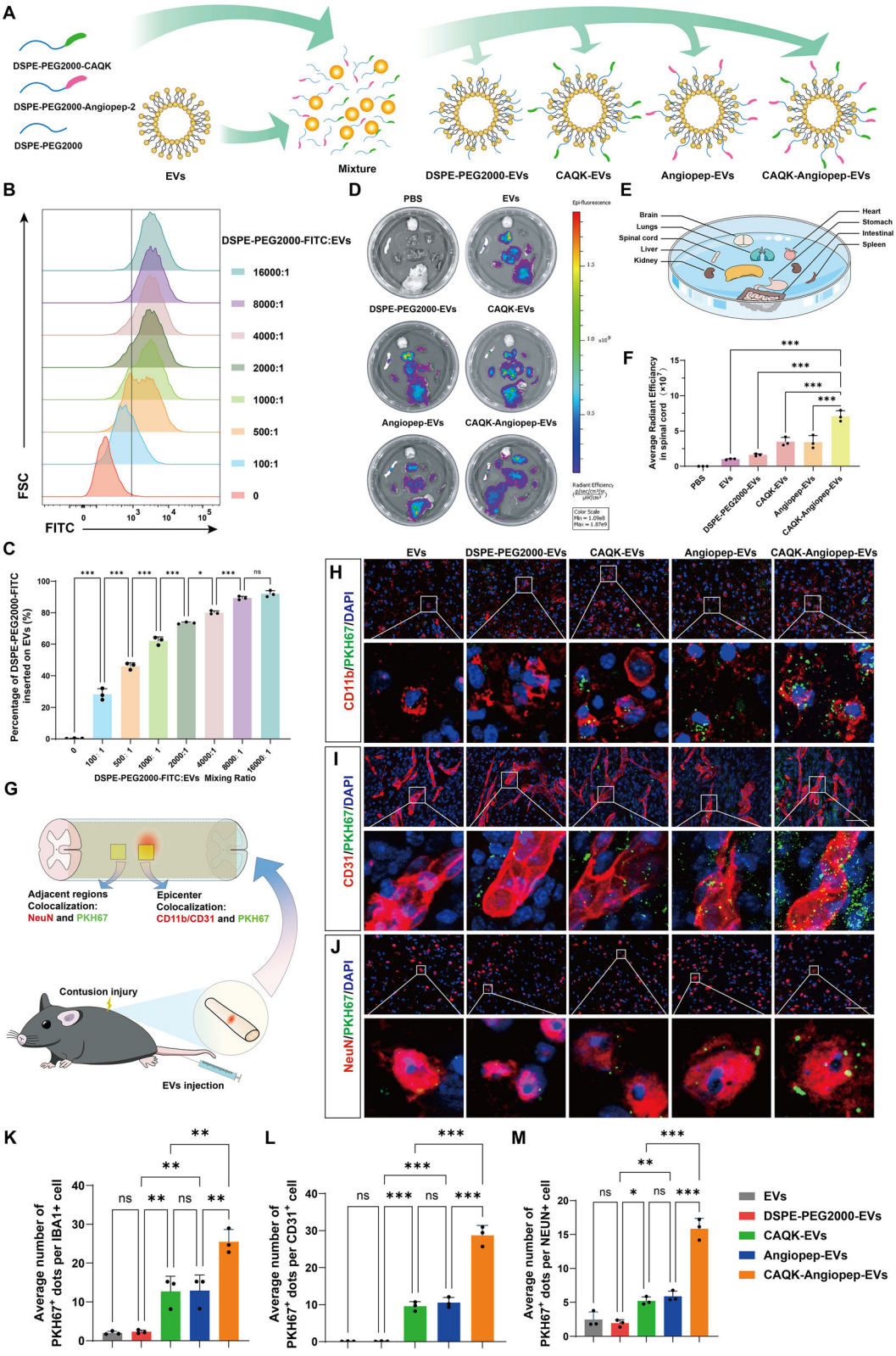

FIGURE 6 | Legend on next page.

SCI repair, with the CAQK-Angiopep2 modification notably enhancing their therapeutic efficacy, presenting encouraging prospects for broadening the clinical utility of EVs in SCI treatment.

4 | Discussion

NSCs are multipotent cells in the central nervous system capable of self-renewal. These cells hold substantial potential in repairing and regenerating neural tissue following injury, as they

20013078, 2025, 7, Downloaded from https://isevjournals.onlinelibrary.wiley.com/doi/10.1002/jev2.70126 by CochraneChina, Wiley Online Library on [27/07/2025]. See the Terms and Conditions (https://onlinelibrary.wiley.com/terms-and-conditions) on Wiley Online Library for rules of use; OA articles are governed by the applicable Creative Commons License

FIGURE 6 | Angiopep2 and CAQK double-labelled EVs exhibit improved targeting specificity to the injury area, internalizing by cells within the injury site. (A) The Schematic of the binding process and the characteristic of the groups. (B) Flow cytometry analysis of DSPE-PEG2000-FITC binding efficiency to EVs. (C) Quantification of the binding rate of the EVs and the FITC labelled targeting peptides. $N = 3$ per group. (D) In vivo tracing of the distribution of DiR-labelled EVs in the injured spinal cord at 24 h post-SCI of the PBS, EVs, DSPE-PEG2000-EVs, CAQK-EVs, Angiopep2-EVs and CAQK-Angiopep2-EVs treated groups. (E) The diagram shows the position of each organ. (F) Quantification of average fluorescence efficiency of (D). $N = 3$ per group. (G) Schematic diagram of the image acquisition site of Figure 6H–J, observing the EV uptake by neuronal cells in the adjacent area of the injury, and observing the EV uptake by microglia and endothelial cells in the injury area. (H) Representative immunofluorescent pictures showing PKH67-labelled EVs (Green) co-labelling with CD11b (Red) at 24 h post SCI. Scale bar, 100 μm. The pictures below show the magnified images in white square region (as indicated). (I) Representative immunofluorescent pictures showing PKH67-labelled EVs (Green) co-labelling with CD31 (Red) at 24 h post SCI. Scale bar, 100 μm. The pictures below show the magnified images in white square region (as indicated). (J) Representative immunofluorescent pictures showing PKH67-labelled EVs (Green) co-labelling with NeuN (Red) at 24 h post SCI. Scale bar, 100 μm. The pictures below show the magnified images in white square region (as indicated). (K–M) Quantification of $PKH67^+$ dots in $CD11b^+$ cells, $CD31^+$ cells and $NeuN^+$ cells in (H–J). Data were collected from three mice per group, with the average number of PKH67+ dots per cell calculated based on three randomly selected fields of view within the region of interest (ROI) of each animal. Data are presented as mean ± SD, NS, no significant difference, $^*p < 0.05$, $^{**}p < 0.01$, $^{***}p < 0.001$.

can differentiate into neurons, oligodendrocytes and astrocytes, contributing to the reconstruction and functional recovery of damaged neural tissues (Zahr et al. 2019). Under neural injury and external stimuli, NSCs can be significantly activated and migrate to damaged areas, facilitating neural regeneration and remyelination (Hosseini et al. 2024; Ceto et al. 2020). However, SCI disrupts the blood–brain barrier and creates inhibitory microenvironments at the injury site, leading to significant apoptosis of transplanted stem cells and hindering their differentiation into neurons and oligodendrocytes, which limits the effectiveness of cell transplantation therapies for SCI (Assinck et al. 2017; Yang et al. 2021). In this study, it was observed that NSCs-transplantation using matrix gel presented challenges such as elevated cell mortality and non-neural differentiation of stem cells, which deviated significantly from our intended experimental objectives. However, through a range of neurological function assessments and histological tests, we discovered that this suboptimal stem cell transplantation remarkably enhanced the efficacy of SCI repair. This implies that, in addition to their role in replacement and repair, transplanted stem cells may contribute to injury recovery through alternative mechanisms.

EVs are nanoscale vesicles produced by various cells that contain bioactive components. They carry diverse cargoes, including lipids, miRNAs, proteins and nucleic acids, and play a crucial role in regulating physiological and pathological processes in the central nervous system (Su et al. 2021; Xia et al. 2022). Studies have shown that transplanted cardiac stem cells release EVs, which are absorbed by cardiomyocytes, reducing myocardial infarct size and promoting cardiac function repair (Saha et al. 2019). Transplanted mesenchymal stem cells have also been reported to release miRNA-containing EVs that facilitate intercellular signalling, promoting neural recovery in ischemic stroke (Heris et al. 2022). Although numerous studies have demonstrated the therapeutic benefits of NSC-transplantation for SCI repair, current research predominantly focuses on the survival of engrafted cells while critically neglecting quantitative documentation of acute-phase apoptosis rates (e.g., temporal dynamics and magnitude of cellular loss within 72 h post-transplantation) (Abematsu et al. 2010; Wang et al. 2023). While acknowledging the inherent neuroregenerative potential of surviving NSCs, this perspective inadequately addresses the pathophysiological reality: most of transplanted NSCs undergo apoptosis within 72 h due to hypoxia and inflammatory stress within the hostile injury microenvironment. Attributing therapeutic effects solely to the residual viable NSCs constitutes an oversimplification of the complex repair mechanisms involving both surviving and hypoxic cellular components. Therefore, elucidating EVs as the key component of NSCs secretome provides a critical breakthrough for deciphering their molecular mechanisms in mediating SCI repair. Our previous research has found that EVs derived from NSCs possess vascular repair capabilities and promote neural regeneration and functional recovery following SCI (Qin et al. 2024; Zhong et al. 2020). In this study, we observed that transplanted stem cells, despite low survival rates and non-neural differentiation, still promote neural function recovery. Utilizing EVs tracing technology and viral labelling, we tracked the secretion of EVs from NSCs post-transplantation. We found that these transplanted NSCs released a substantial number of EVs, which were subsequently taken up by neurons, microglia, and vascular endothelial cells. Notably, inhibiting the secretion of these EVs significantly diminished the therapeutic effects of NSC transplantation on SCI repair. But it is also worth noting that at 56 days post transplantation, a large number of EGFP-positive labelled cells were still detected in the injured area in this study. Although these cells are mainly differentiated into astrocytes, such cells may still play an active repair role, including inhibiting tissue scar formation and promoting nerve regeneration, and so forth (Anderson et al. 2016; Walczak et al. 2011; Sandrock et al. 2010; Noble et al. 2011). Thus, it remains clearly inadequate to elucidate the reparative mechanisms of stem cell transplantation for SCI solely through the EVs derived from transplanted NSCs highlighted in this study. While the current study has not yet elucidated the precise mechanisms underlying transplanted NSCs-derived astrocytes, a systematic investigation of their proliferation dynamics, differentiation trajectories, and microenvironmental interactions will prove crucial for identifying pivotal regulatory checkpoints in SCI repair, which also has significant scientific value for guiding the clinical transformation of SCI treatment.

After SCI, a hypoxic microenvironment forms due to disrupted blood supply and reduced local blood flow. This hypoxic condition triggers a series of complex pathophysiological responses, including neuronal death, inflammation and impaired tissue repair (Zrzavy et al. 2021). Hypoxia also activates various cellular stress response pathways, such as the HIF signalling pathway, further impacting cell survival and function (Chang et al. 2019;

20013078, 2025, 7, Downloaded from https://isevjournals.onlinelibrary.wiley.com/doi/10.1002/jev2.70126 by CochraneChina, Wiley Online Library on [27/07/2025]. See the Terms and Conditions (https://onlinelibrary.wiley.com/terms-and-conditions) on Wiley Online Library for rules of use; OA articles are governed by the applicable Creative Commons License

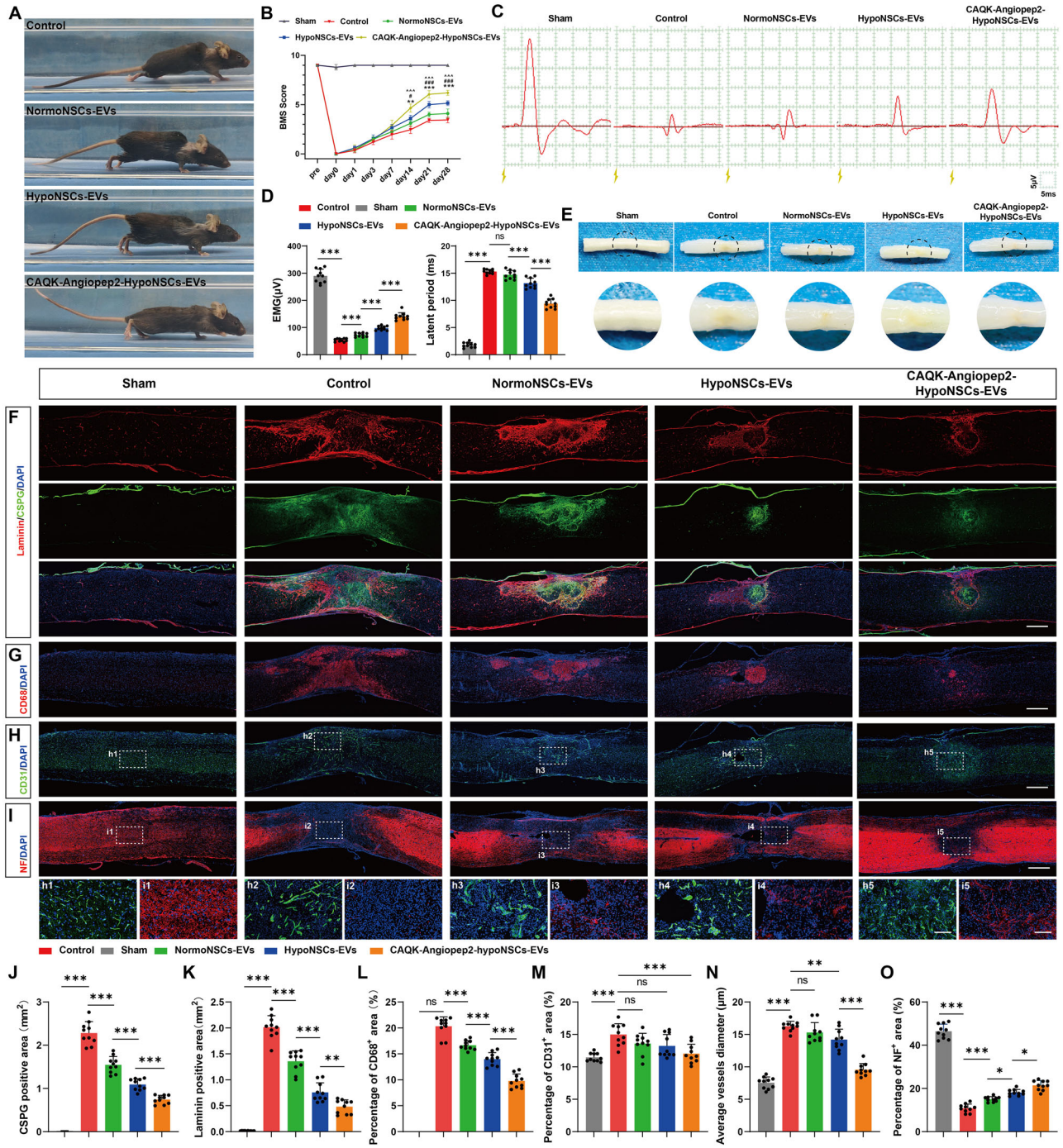

FIGURE 7 | Legend on next page.

Rosenberger et al. 2006). Meanwhile, under hypoxic conditions, cells experience substantial alterations in their environment. To adapt, cells often adjust their metabolic and signalling pathways. One such adaptation involves regulating the quantity and biological composition of the EVs release (Bister et al. 2020; Ren et al. 2019). Research has demonstrated that hypoxic conditions in various tumour diseases can significantly affect the secretion and function of EVs, which are crucial for tumour angiogenesis, invasion, metastasis, and immune regulation. And previous research has shown that hypoxia-treatment could induce EVs releasing from microglia, neural cells and pluripotent stem cells for generating a regenerative phenotype (Xin et al. 2023; Paw et al. 2023; Korvenlaita et al. 2023). This phenomenon aligns mechanistically with our quantitative NTA profiling, which demonstrated a double fold increase in EVs secretion from hypoxic NSCs compared to normoxic controls. One of the known mechanisms for EVs biogenesis involves the recruitment of the membrane anchored Ras superfamily of small G proteins (RABs) for membrane budding and fusion processes (Wilmes and Kümmel 2023). HIFs were shown to directly bind to the RAB22A promoter and to induce the expression of RAB22A. And silencing RAB22A expression prevented the hypoxia-induced EVs releasing (Wang et al. 2014). Direct binding of HIF-1α to the RAB27A promoter has been described in B cells and the observed increased

20013078, 2025, 7, Downloaded from https://isevjournals.onlinelibrary.wiley.com/doi/10.1002/jev2.70126 by CochraneChina, Wiley Online Library on [27/07/2025]. See the Terms and Conditions (https://onlinelibrary.wiley.com/terms-and-conditions) on Wiley Online Library for rules of use; OA articles are governed by the applicable Creative Commons License

FIGURE 7 | CAQK and Angiopep2 co-modification EVs significantly promoted functional recovery post SCI. (A) Representative pictures are showing hindlimb movement of mice at 4 weeks after spinal cord contusion and treatment. (B) BMS scores in sham, control, NormoNSCs-EVs, HypoNSCs-EVs and CAQK-Angiopep2-HypoNSCs-EVs treated groups at different time points post-SCI. $N = 10$ per group. * Control versus NormoNSCs-EVs groups; # NormoNSCs-EVs versus HypoNSCs-EVs; ^ HypoNSCs-EVs versus CAQK-Angiopep2-HypoNSCs-EVs. (C) Representative electrophysiological trace images were recorded in each group at 8 weeks post-SCI. (D) Measurement of the MEP amplitude and latent period in (C). (E) Photographic presentation of the isolated spinal cord in sham, control, NormoNSCs-EVs, HypoNSCs-EVs and CAQK-Angiopep2-HypoNSCs-EVs treated groups. (F) Representative immunofluorescent stains of the scar tissue (CSPG, green fluoresce, Laminin, Red fluoresces) images of the spinal cord at 8 weeks post-injury in each group. Scale bar, 500 μm. (G) Representative immunofluorescent stains of CD68 (Red fluoresce) images of the spinal cord at 8 weeks post-injury in each group. Scale bar, 500 μm. (g1–g6) Higher magnification of inflammatory cells in dotted boxes as indicated in (G). Scale bar: 100 μm. (H) Representative immunofluorescent stains of CD31 (Green fluoresce) images of the spinal cord at 8 weeks post-injury in each group. Scale bar, 500 μm. (h1–h6) Higher magnification of remodelling vessels in dotted boxes as indicated in (I). Scale bar: 100 μm. (I) Representative immunofluorescent stains of NF (Red fluoresce) images of the spinal cord at 8 weeks post-injury in each group. Scale bar, 500 μm. (i1-i6) Higher magnification of regenerative neural fibres in dotted boxes as indicated in (I). Scale bar: 100 μm. (J) Quantification of CSPG positive signals in the epicentre of sham, control, NormoNSCs-EVs, HypoNSCs-EVs and CAQK-Angiopep2-HypoNSCs-EVs treated mice in (F). (K) Quantification of Laminin positive signals in the epicentre of sham, control, NormoNSCs-EVs, HypoNSCs-EVs and CAQK-Angiopep2-HypoNSCs-EVs treated mice in (F). (L) Quantification of CD68 positive signals the epicentre of in sham, control, NormoNSCs-EVs, HypoNSCs-EVs and CAQK-Angiopep2-HypoNSCs-EVs treated mice in (G). (M) Quantification of CD31 positive signals in the epicentre of sham, control, NormoNSCs-EVs, HypoNSCs-EVs and CAQK-Angiopep2-HypoNSCs-EVs treated mice in (H). (N) Average vessels diameter quantification of CD31 positive vascular in the epicentre of sham, control, NormoNSCs-EVs, HypoNSCs-EVs and CAQK-Angiopep2-HypoNSCs-EVs treated mice in (H). (O) Quantification of NF positive signals in the epicentre of sham, control, NormoNSCs-EVs, HypoNSCs-EVs and CAQK-Angiopep2-HypoNSCs-EVs treated mice in (I). Data are presented as mean ± SD, NS, no significant difference, $^{*}p < 0.05$, $^{**}p < 0.01$, $^{***}p < 0.001$.

release of EVs due to hypoxia was shown to be dependent on this process (Zhang et al. 2019). In this study, through RNA-seq analysis of hypoxic NSCs, we found that with the activation of the HIF-1α signalling pathway, the expression of Rab17 significantly increased, indicating that hypoxia significantly increased the generation of EVs in NSCs. This reveals that hypoxic NSCs can enhance the paracrine effect by strengthening the EV release function, regulating the biological functions of target cells. Based on the knockdown of Rab17, we also found that after Rab17 knockdown, the EV secretion function of these NSCs weakened, further resulting in the deterioration of the therapeutic effect of NSC transplantation.

And the content of hypoxic EVs can be altered by hypoxia induction. Recent studies showed that isolated EVs from hypoxia induced MSCs and found that the EVs contained a number of pro-angiogenic factors that may be beneficial to ischemic tissues (Sun et al. 2020; Zhu et al. 2018). Studies have shown the improved effectiveness of EVs released by hypoxia-preconditioned stem cells in promoting SCI repair. For instance, EVs released by hypoxia-induced mesenchymal stem cells have been demonstrated to enhance SCI recovery by promoting microglial polarization toward the anti-inflammatory phenotype through the delivery of miR-216a-5p, consequently enhancing neural function. Moreover, a separate study demonstrated that EVs derived from hypoxia-induced adipose-derived mesenchymal stem cells carry miR-499a-5p, which, upon internalization by neurons, mitigates neuronal apoptosis and promotes neural repair by inhibiting the JNK3/c-JUN signalling pathway (Liang et al. 2022). These investigations suggest that hypoxia preconditioning not only amplifies the secretion of stem cell EVs but also modifies their biological composition, augmenting their efficacy in promoting neural repair. In this study, by performing proteomic analysis on two types of EVs, it was found that a serials of cytokines were enriched expressed in hypoNSCs-EVs, such as such as Ccndl, Adnp and Hsp90aa1 exhibit significant neural regenerative potential, Vegfa, Pdcl3 and Hsp90ab1 are associated with promoting angiogenesis, and proteins like Atf7ip play a role in anti-inflammatory processes (Hu et al. 2024; Hagey et al. 2020; Gozes et al. 2015; Sun et al. 2020; Sin et al. 2019). And the functional enrichment analysis revealed that the upregulated proteins in hypoNSCs-EVs are primarily involved in protein folding and stability, inhibition of neuronal apoptosis, promotion of axonal growth, and activation of the VEGFR pathway, which was closely related to the repair of SCI. Combining in vitro and in vivo study of the hypoNSCs-EVs, it found that co-culturing HypoNSC-EVs with neurons, microglia, and endothelial cells significantly promotes axonal regeneration and vascular regeneration, reduces neuroinflammation, and ultimately promotes neural function recovery. Consequently, leveraging hypoxia preconditioning to enhance the therapeutic potential of stem cell EVs presents a novel avenue for research and a promising therapeutic strategy for SCI repair.

Traditional stem cell transplantation is limited in clinical applications due to issues such as immune rejection, difficulty in controlling differentiation and proliferation, low cell survival rates, technical challenges and ethical concerns (Yang et al. 2024; Zeng 2023). In contrast, EVs therapy can avoid the immune reactions associated with stem cell transplantation, reduce potential tumorigenic risks, and facilitate long-term storage. However, simple intravenous administration of EVs may result in extensive metabolism by the liver and kidneys, with only a small fraction of EVs reaching the SCI site, significantly limiting the therapeutic effectiveness of EVs for SCI (Barile and Vassalli 2017; Akbari et al. 2020). Therefore, this study focused on identifying effective methods to achieve targeted delivery of EVs to injury sites with improved accuracy. Currently, the development and application of targeting peptides have endowed EVs with new characteristics. Compared to other drug carriers, targeting peptides have higher targeting specificity, stronger affinity for targets, and can be administered intravenously, further enhancing their clinical translational value (Zhou et al. 2021; Meloni et al. 2015). The CAQK peptide is related to extracellular matrix components and

20013078, 2025, 7, Downloaded from https://isevjournals.onlinelibrary.wiley.com/doi/10.1002/jev2.70126 by CochraneChina, Wiley Online Library on [27/07/2025]. See the Terms and Conditions (https://onlinelibrary.wiley.com/terms-and-conditions) on Wiley Online Library for rules of use; OA articles are governed by the applicable Creative Commons License

can target demyelinated injury sites (Abi-Ghanem et al. 2022). Our previous research showed that the CAQK peptide effectively targeted demyelinated injury sites, efficiently delivering mitochondria to the SCI area (Xu et al. 2024). Angiopep2 has been shown to be an active targeting peptide with high affinity for low-density lipoprotein receptor-related protein-1 and the ability to penetrate the blood–brain barrier, making it particularly promising for the treatment of central nervous system diseases (Zhu et al. 2022; Habib and Singh 2022). In this study, we engineered hypoxia-preconditioned NSC-EVs integrated with dual-targeting peptides (CAQK and Angiopep2), demonstrating that this combinatorial targeting approach achieves synergistic effects to significantly enhance EV tropism toward injury sites while maintaining intrinsic biocompatibility. This engineered platform offers a novel strategy for developing precision-targeted drug delivery systems in post-SCI therapeutic interventions.

In this study, we initiated our research with an experiment on stem cell transplantation for the treatment of SCI. Although the survival rate and neural differentiation of the transplanted cells did not meet expectations, their reparative influence on SCI was undeniably profound. This unexpected finding prompted us to delve deeper into the role of extracellular factors in stem cell transplantation. We discovered that hypoxia, as a stress factor, could induce the release of a substantial volume of EVs from stem cells through the HIF-1α/RAB17 pathway, and promoted the generation of beneficial cytokines, which are instrumental in the reparative process of SCI. Building upon this discovery, we demonstrated that EVs harvested from hypoxic NSCs, when conjugated with the CAQK/Angiopep2 targeting peptides, could be precisely navigated to the site of injury and exerted a stronger role in promoting SCI repair. And, considering that the spinal cord complete transection model causes extensive damage, it is difficult to achieve perfect repair of a 2-mm spinal cord tissue defect through endogenous nerve tissue regeneration. Therefore, this animal model is more suitable for evaluating the efficacy of treatments such as tissue engineering scaffolds or cell transplantation. The spinal cord contusion model, on the other hand, is more consistent with the common clinical injury patterns. The lesion centre is mainly characterized by pathological phenomena such as haemorrhage, inflammation and nerve injury-induced apoptosis. The spinal cord tissue has a certain self-repair ability, and this model is often used to simply evaluate the efficacy of EVs, thus being more in line with the goals of our subsequent research. Based on the above considerations, we used the spinal cord contusion model for the efficacy evaluation of EVs. Therefore, by leveraging these complementary animal models, we systematically investigated the post-transplantation biodistribution and repair mechanisms of NSCs, ultimately developing an innovative hypoxia-conditioned EV engineering approach. This breakthrough establishes a novel cell-free targeted therapeutic paradigm for SCI treatment, combining precise delivery with endogenous regeneration potential.

5 | Conclusions

Our investigation elucidated the reparative functions and underlying mechanisms of transplanted NSCs in SCI, with a particular emphasis on their non-cellular contributions and identified EVs as a pivotal factor influencing the efficacy of NSC transplantation, which is modulated by the HIF1-α/RAB17 pathway. Leveraging these insights, we have crafted an innovative and targeted strategy for the transplantation of EVs derived from NSCs. This study presents a cell-free, precision therapeutic intervention for SCI treatment, potentially revolutionizing the field of regenerative medicine.

Author Contributions

Tian Qin: Methodology (equal), visualization (equal), writing – original draft (equal), writing – review and editing (equal). **Yiming Qin**: Methodology (equal), visualization (equal), writing – original draft (equal), writing – review and editing (equal). **Haicheng Wen**: Methodology (equal), software (equal). **Tianding Wu**: Investigation (equal), project administration (equal). **chunyue duan**: Investigation (equal), project administration (equal). **Yong Cao**: Formal analysis (equal), investigation (equal). **Yi Sun**: Software (equal). **Hongkang Zhou**: Software (supporting). **Hongbin Lu**: Funding acquisition (equal), writing – review and editing (equal). **Liyuan Jiang**: Data curation (equal), methodology (equal). **Jianzhong Hu**: Funding acquisition (equal), writing – review and editing (equal). **Chengjun Li**: Funding acquisition (equal), project administration (lead).

Acknowledgements

This work was funded by the National Natural Science Foundation of China (grant 82030071), the Science and Technology Major Project of Changsha, China (NO. kh2103008) and Hunan Province Graduate Research Innovation Project (CX20230379), the Natural Science Foundation Project of Hunan Province (2024JJ6637), the Natural Science Foundation Project of Changsha (kq2403018) and the Youth Fund Scientific Research Project of Xiangya Hospital (2023Q05).

Conflicts of Interest

The authors declare that they have no competing interests.

Data Availability Statement

The data that supports the findings of this study are available in the supplementary material of this article

References

Abematsu, M., K. Tsujimura, M. Yamano, et al. 2010. "Neurons Derived From Transplanted Neural Stem Cells Restore Disrupted Neuronal Circuitry in a Mouse Model of Spinal Cord Injury." *Journal of Clinical Investigation* 120, no. 9: 3255–3266.

Abi-Ghanem, C., D. Jonnalagadda, J. Chun, Y. Kihara, and B. Ranscht. 2022. "CAQK, A Peptide Associating With Extracellular Matrix Components Targets Sites of Demyelinating Injuries." *Frontiers in Cellular Neuroscience* 16: 908401.

Ahuja, C. S., J. R. Wilson, S. Nori, et al. 2017. "Traumatic Spinal Cord Injury." *Nature Reviews Disease Primers* 3: 17018.

Akbari, A., N. Jabbari, R. Sharifi, et al. 2020. "Free and Hydrogel Encapsulated Exosome-Based Therapies in Regenerative Medicine." *Life Sciences* 249: 117447.

Anderson, M. A., J. E. Burda, Y. Ren, et al. 2016. "Astrocyte Scar Formation Aids central Nervous System Axon Regeneration." *Nature* 532, no. 7598: 195–200.

Assinck, P., G. J. Duncan, B. J. Hilton, J. R. Plemel, and W. Tetzlaff. 2017. "Cell Transplantation Therapy for Spinal Cord Injury." *Nature Neuroscience* 20, no. 5: 637–647.

20013078, 2025, 7, Downloaded from https://isevjournals.onlinelibrary.wiley.com/doi/10.1002/jev2.70126 by CochraneChina, Wiley Online Library on [27/07/2025]. See the Terms and Conditions (https://onlinelibrary.wiley.com/terms-and-conditions) on Wiley Online Library for rules of use; OA articles are governed by the applicable Creative Commons License

Barile, L., and G. Vassalli. 2017. "Exosomes: Therapy Delivery Tools and Biomarkers of Diseases." *Pharmacology & Therapeutics* 174: 63–78.

Basso, D. M., L. C. Fisher, A. J. Anderson, L. B. Jakeman, D. M. Mctigue, and P. G. Popovich. 2006. "Basso Mouse Scale for Locomotion Detects Differences in Recovery After Spinal Cord Injury in Five Common Mouse Strains." *Journal of Neurotrauma* 23, no. 5: 635–659.

Bister, N., C. Pistono, B. Huremagic, J. Jolkkonen, R. Giugno, and T. Malm. 2020. "Hypoxia and Extracellular Vesicles: A Review On Methods, Vesicular Cargo and Functions." *Journal of Extracellular Vesicles* 10, no. 1: e12002.

Ceto, S., K. J. Sekiguchi, Y. Takashima, A. Nimmerjahn, and M. H. Tuszynski. 2020. "Neural Stem Cell Grafts Form Extensive Synaptic Networks That Integrate With Host Circuits After Spinal Cord Injury." *Cell Stem Cell* 27, no. 3: 430–440.e5.

Chang, J., B. Yang, Y. Zhou, et al. 2019. "Acute Methylmercury Exposure and the Hypoxia-Inducible Factor-1α Signaling Pathway Under Normoxic Conditions in the Rat Brain and Astrocytes In Vitro." *Environmental Health Perspectives* 127, no. 12: 127006.

Chen, C.-Y., S.-S. Rao, L. U. Ren, et al. 2018. "Exosomal DMBT1 From Human Urine-Derived Stem Cells Facilitates Diabetic Wound Repair by Promoting Angiogenesis." *Theranostics* 8, no. 6: 1607–1623.

Chen, D., L. Zhou, G. Chen, et al. 2024. "FUNDC1-Induced Mitophagy Protects Spinal Cord Neurons Against Ischemic Injury." *Cell Death Discovery* 10, no. 1: 4.

Chen, W., L. Zhang, G. Zhong, et al. 2024. "Regulation of Microglia Inflammation and Oligodendrocyte Demyelination by Engeletin via the TLR4/RRP9/NF-κB Pathway After Spinal Cord Injury." *Pharmacological Research* 209: 107448.

Festa, B. P., F. H. Siddiqi, M. Jimenez-Sanchez, et al. 2023. "Microglial-to-Neuronal CCR5 Signaling Regulates Autophagy in Neurodegeneration." *Neuron* 111: 2021–2037.e12.

GBD 2016. 2019. "Traumatic Brain Injury and Spinal Cord Injury Collaborators, Global, Regional, and National Burden of Traumatic Brain Injury and Spinal Cord Injury, 1990–2016: A Systematic Analysis for the Global Burden of Disease Study 2016." *Lancet Neurology* 18, no. 1: 56–87.

Gozes, I., A. Yeheskel, and M. Pasmanik-Chor. 2015. "Activity-Dependent Neuroprotective Protein (ADNP): A Case Study for Highly Conserved Chordata-Specific Genes Shaping the Brain and Mutated in Cancer." *Journal of Alzheimer's Disease* 45, no. 1: 57–73.

Habib, S., and M. Singh. 2022. "Angiopep-2-Modified Nanoparticles for Brain-Directed Delivery of Therapeutics: A Review." *Polymers (Basel)* 14, no. 4: 712.

Hagey, D. W., D. Topcic, N. Kee, et al. 2020. "CYCLIN-B1/2 and -D1 Act in Opposition to Coordinate Cortical Progenitor Self-Renewal and Lineage Commitment." *Nature Communications* 11, no. 1: 2898.

Heris, R. M., M. Shirvaliloo, S. Abbaspour-Aghdam, et al. 2022. "The Potential Use of Mesenchymal Stem Cells and Their Exosomes in Parkinson's Disease Treatment." *Stem Cell Research & Therapy* 13, no. 1: 371.

Hill, A. F. 2019. "Extracellular Vesicles and Neurodegenerative Diseases." *Journal of Neuroscience* 39, no. 47: 9269–9273.

Hosseini, S. M., B. Borys, and S. Karimi-Abdolrezaee. 2024. "Neural Stem Cell Therapies for Spinal Cord Injury Repair: an Update On Recent Preclinical and Clinical Advances." *Brain* 147, no. 3: 766–793.

Hu, S., Y. Tang, X. Li, et al. 2024. "Hsp90aa1/JUN/Ccl2 Regulatory Axis Mediates Migration and Differentiation of NSPCs, Promoting the Onset and Progression of Early Post-Ischemic Stroke Epilepsy." *Neurobiology of Disease* 200: 106635.

Hu, X., W. Xu, Y. Ren, et al. 2023. "Spinal Cord Injury: Molecular Mechanisms and Therapeutic Interventions." *Signal Transduction and Targeted Therapy* 8, no. 1: 245.

Huang, H., L. Chen, G. Moviglia, et al. 2022. "Advances and Prospects of Cell Therapy for Spinal Cord Injury Patients." *Journal of Neurorestoratology* 10, no. 1: 13–30.

John, R. K., S. P. Vogel, S. Zia, et al. 2025. "Reawakening Inflammation in the Chronically Injured Spinal Cord Using Lipopolysaccharide Induces Diverse Microglial States." *Journal of Neuroinflammation* 22, no. 1: 56.

Korvenlaita, N., M. Gómez-Budia, F. Scoyni, et al. 2023. "Dynamic Release of Neuronal Extracellular Vesicles Containing miR-21a-5p Is Induced by Hypoxia." *Journal of Extracellular Vesicles* 12, no. 1: e12297.

Kumar, M. A., S. K. Baba, H. Q. Sadida, et al. 2024. "Extracellular Vesicles as Tools and Targets in Therapy for Diseases." *Signal Transduction and Targeted Therapy* 9, no. 1: 27.

LaGory, E. L., and A. J. Giaccia. 2016. "The Ever-Expanding Role of HIF in Tumour and Stromal Biology." *Nature Cell Biology* 18, no. 4: 356–365.

Lan, X. I., X. Han, Q. Li, Q.-W. U. Yang, and J. Wang. 2017. "Modulators of Microglial Activation and Polarization After Intracerebral Haemorrhage." *Nature Reviews Neurology* 13, no. 7: 420–433.

Lee, M., E. S. U. Lee, Y. S. Kim, et al. 2005. "Ischemic Injury-Specific Gene Expression in the Rat Spinal Cord Injury Model Using Hypoxia-Inducible System." *Spine (Phila Pa 1976)* 30, no. 24: 2729–2734.

Liang, H.-B., X. Chen, R. Zhao, et al. 2024. "Simultaneous Ischemic Regions Targeting and BBB Crossing Strategy to Harness Extracellular Vesicles for Therapeutic Delivery in Ischemic Stroke." *Journal of Controlled Release* 365: 1037–1057.

Liang, Y., J.-H. Wu, J.-H. Zhu, and H. Yang. 2022. "Exosomes Secreted by Hypoxia-Pre-Conditioned Adipose-Derived Mesenchymal Stem Cells Reduce Neuronal Apoptosis in Rats With Spinal Cord Injury." *Journal of Neurotrauma* 39, no. 9-10: 701–714.

Liu, W.-Z., Z. J. Ma, J. R. Li, and X. W. Kang. 2021. "Mesenchymal Stem Cell-Derived Exosomes: Therapeutic Opportunities and Challenges for Spinal Cord Injury." *Stem Cell Research & Therapy* 12, no. 1: 102.

Lu, P., Y. Wang, L. Graham, et al. 2012. "Long-Distance Growth and Connectivity of Neural Stem Cells After Severe Spinal Cord Injury." *Cell* 150, no. 6: 1264–1273.

Mathieu, M., N. Névo, M. Jouve, et al. 2021. "Specificities of Exosome Versus Small Ectosome Secretion Revealed by Live Intracellular Tracking of CD63 and CD9." *Nature Communications* 12, no. 1: 4389.

Meloni, B. P., D. Milani, A. B. Edwards, et al. 2015. "Neuroprotective Peptides Fused to Arginine-Rich Cell Penetrating Peptides: Neuroprotective Mechanism Likely Mediated by Peptide Endocytic Properties." *Pharmacology & Therapeutics* 153: 36–54.

Najem, H., S. T. Lea, S. Tripathi, et al. 2024. "STING Agonist 8803 Reprograms the Immune Microenvironment and Increases Survival in Preclinical Models of Glioblastoma." *Journal of Clinical Investigation* 134, no. 12: e175033.

Noble, M., J. E. Davies, M. Mayer-Pröschel, C. Pröschel, and S. J. A. Davies. 2011. "Precursor Cell Biology and the Development of Astrocyte Transplantation Therapies: Lessons From Spinal Cord Injury." *Neurotherapeutics* 8, no. 4: 677–693.

Okabe, M., M. Ikawa, K. Kominami, T. Nakanishi, and Y. Nishimune. 1997. "'Green Mice' as a Source of Ubiquitous Green Cells." *FEBS Letters* 407, no. 3: 313–319.

Paw, M., A. A. Kusiak, K. Nit, et al. 2023. "Hypoxia Enhances Anti-Fibrotic Properties of Extracellular Vesicles Derived From hiPSCs via the miR302b-3p/TGFβ/SMAD2 Axis." *BMC Medicin* 21, no. 1: 412.

Pužar Dominkuš, P., M. ž Stenovec, S. Sitar, et al. 2018. "PKH26 Labeling of Extracellular Vesicles: Characterization and Cellular Internalization of Contaminating PKH26 Nanoparticles." *Biochimica Et Biophysica Acta (BBA)—Biomembranes* 1860, no. 6: 1350–1361.

Qin, T., C. Li, Y. Xu, et al. 2024. "Local Delivery of EGFR+NSCs-Derived Exosomes Promotes Neural Regeneration Post Spinal Cord Injury via miR-34a-5p/HDAC6 Pathway." *Bioactive Materials* 33: 424–443.

20013078, 2025, 7, Downloaded from https://isevjournals.onlinelibrary.wiley.com/doi/10.1002/jev2.70126 by CochraneChina, Wiley Online Library on [27/07/2025]. See the Terms and Conditions (https://onlinelibrary.wiley.com/terms-and-conditions) on Wiley Online Library for rules of use; OA articles are governed by the applicable Creative Commons License

Ransohoff, R. M. 2016. "A Polarizing Question: Do M1 and M2 Microglia Exist?." *Nature Neuroscience* 19, no. 8: 987–991.

Rattner, A., J. Williams, and J. Nathans. 2019. "Roles of HIFs and VEGF in Angiogenesis in the Retina and Brain." *Journal of Clinical Investigation* 129, no. 9: 3807–3820.

Ren, W., J. Hou, C. Yang, et al. 2019. "Extracellular Vesicles Secreted by Hypoxia Pre-Challenged Mesenchymal Stem Cells Promote Non-Small Cell Lung Cancer Cell Growth and Mobility as Well as Macrophage M2 Polarization via miR-21-5p Delivery." *Journal of Experimental & Clinical Cancer Research* 38, no. 1: 62.

Ribeiro, B. F., B. C. Da Cruz, B. M. De Sousa, et al. 2023. "Cell Therapies for Spinal Cord Injury: A Review of the Clinical Trials and Cell-Type Therapeutic Potential." *Brain* 146, no. 7: 2672–2693.

Rosenberger, C., S. Rosen, A. Shina, et al. 2006. "Hypoxia-Inducible Factors and Tubular Cell Survival in Isolated Perfused Kidneys." *Kidney International* 70, no. 1: 60–70.

Saha, P., S. Sharma, L. Korutla, et al. 2019. "Circulating Exosomes Derived From Transplanted Progenitor Cells Aid the Functional Recovery of Ischemic Myocardium." *Science Translational Medicine* 11, no. 493: eaau1168.

Sandrock, R. W., W. Wheatley, C. Levinthal, et al. 2010. "Isolation, Characterization and Preclinical Development of Human Glial-Restricted Progenitor Cells for Treatment of Neurological Disorders." *Regenerative Medicine* 5, no. 3: 381–394.

Schito, L., S. Rey, M. Tafani , et al. 2012. "Hypoxia-Inducible Factor 1-Dependent Expression of Platelet-Derived Growth Factor B Promotes Lymphatic Metastasis of Hypoxic Breast Cancer Cells." *Proceedings of the National Academy of Sciences USA* 109, no. 40: E2707–E2716.

Semenza, G. L. 2000. "Surviving Ischemia: Adaptive Responses Mediated by Hypoxia-Inducible Factor 1." *Journal of Clinical Investigation* 106, no. 7: 809–812.

Sin, J. H., C. Zuckerman, J. T. Cortez, et al. 2019. "The Epigenetic Regulator ATF7ip Inhibits Il2 Expression, Regulating Th17 Responses." *Journal of Experimental Medicine* 216, no. 9: 2024–2037.

Su, H., Y. H. Rustam, C. L. Masters, et al. 2021. "Characterization of Brain-Derived Extracellular Vesicle Lipids in Alzheimer's Disease." *Journal of Extracellular Vesicles* 10, no. 7: e12089.

Sun, J., H. Shen, L. Shao, et al. 2020. "HIF-1α Overexpression in Mesenchymal Stem Cell-Derived Exosomes Mediates Cardioprotection in Myocardial Infarction by Enhanced Angiogenesis." *Stem Cell Res Therapy* 11, no. 1: 373.

Sun, X., X. Peng, Y. Cao, Y. Zhou, and Y. Sun. 2020. "ADNP Promotes Neural Differentiation by Modulating Wnt/β-Catenin Signaling." *Nature Communications* 11, no. 1: 2984.

Takov, K., D. M. Yellon, and S. M. Davidson. 2017. "Confounding Factors in Vesicle Uptake Studies Using Fluorescent Lipophilic Membrane Dyes." *Journal of Extracellular Vesicles* 6, no. 1: 1388731.

van Niel, G., G. D'Angelo, and G. Raposo. 2018. "Shedding Light on the Cell Biology of Extracellular Vesicles." *Nature Reviews. Molecular Cell Biology* 19, no. 4: 213–228.

Walczak, P., A. H. All, N. Rumpal, et al. 2011. "Human Glial-Restricted Progenitors Survive, Proliferate, and Preserve Electrophysiological Function in Rats With Focal Inflammatory Spinal Cord Demyelination." *Glia* 59, no. 3: 499–510.

Wang, R., X. Wu, Z. Tian , et al. 2023. "Sustained Release of Hydrogen Sulfide From Anisotropic Ferrofluid Hydrogel for the Repair of Spinal Cord Injury." *Bioactive Materials* 23: 118–128.

Wang, T., D. M. Gilkes, N. Takano , et al. 2014. "Hypoxia-Inducible Factors and RAB22A Mediate Formation of Microvesicles That Stimulate Breast Cancer Invasion and Metastasis." *Proceedings of the National Academy of Sciences USA* 111, no. 31: E3234–E3242.

Wang, Y., T. Zhao, Y. Jiao, et al. 2023. "Silicate Nanoplatelets Promotes Neuronal Differentiation of Neural Stem Cells and Restoration of Spinal Cord Injury." *Advanced Healthcare Materials* 12, no. 19: e2203051.

Wilmes, S., and D. Kümmel. 2023. "Insights Into the Role of the Membranes in Rab GTPase Regulation." *Current Opinion In Cell Biology* 83: 102177.

Xia, X., Y. Wang, and J. C. Zheng. 2022. "Extracellular Vesicles, From the Pathogenesis to the Therapy of Neurodegenerative Diseases." *Translational Neurodegeneration* 11, no. 1: 53.

Xin, W., Y. Pan, W. Wei, et al. 2023. "Preconditioned Extracellular Vesicles From Hypoxic Microglia Reduce Poststroke AQP4 Depolarization, Disturbed Cerebrospinal Fluid Flow, Astrogliosis, and Neuroinflammation." *Theranostics* 13, no. 12: 4197–4216.

Xu, J., C. Shi, F. Yuan , et al. 2024. "Targeted Transplantation of Engineered Mitochondrial Compound Promotes Functional Recovery After Spinal Cord Injury by Enhancing Macrophage Phagocytosis." *Bioactive Materials* 32: 427–444.

Xu, R., D. W. Greening, H.-J. Zhu, N. Takahashi, and R. J. Simpson. 2016. "Extracellular Vesicle Isolation and Characterization: Toward Clinical Application." *Journal of Clinical Investigation* 126, no. 4: 1152–1162.

Xue, W., C. Fan, B. Chen, Y. Zhao, Z. Xiao, and J. Dai. 2021. "Direct Neuronal Differentiation of Neural Stem Cells for Spinal Cord Injury Repair." *Stem Cells* 39, no. 8: 1025–1032.

Yang, Y., Y. Fan, H. Zhang, et al. 2021. "Small Molecules Combined With Collagen Hydrogel Direct Neurogenesis and Migration of Neural Stem Cells After Spinal Cord Injury." *Biomaterials* 269: 120479.

Yang, Y., B. Ma, J. Chen, et al. 2024. "Epigenetic Regulation and Factors That Influence the Effect of iPSCs-Derived Neural Stem/Progenitor Cells (NS/PCs) in the Treatment of Spinal Cord Injury." *Clinical Epigenetics* 16, no. 1: 30.

You, Z., X. U. Gao, X. Kang, et al. 2023. "Microvascular Endothelial Cells Derived From Spinal Cord Promote Spinal Cord Injury Repair." *Bioactive Materials* 29: 36–49.

Zahr, S. K., D. R. Kaplan, and F. D. Miller. 2019. "Translating Neural Stem Cells to Neurons in the Mammalian Brain." *Cell Death and Differentiation* 26, no. 12: 2495–2512.

Zeng, C. W. 2023. "Advancing Spinal Cord Injury Treatment Through Stem Cell Therapy: A Comprehensive Review of Cell Types, Challenges, and Emerging Technologies in Regenerative Medicine." *International Journal of Molecular Sciences* 24, no. 18: 14349.

Zhang, B., R. Yeo, K. Tan, and S. Lim. 2016. "Focus on Extracellular Vesicles: Therapeutic Potential of Stem Cell-Derived Extracellular Vesicles." *International Journal of Molecular Sciences* 17, no. 2: 174.

Zhang, F., R. Li, Y. Yang, et al. 2019. "Specific Decrease in B-Cell-Derived Extracellular Vesicles Enhances Post-Chemotherapeutic CD8(+) T Cell Responses." *Immunity* 50, no. 3: 738–750.e7.

Zhong, D., Y. Cao, C.-J. Li, et al. 2020. "Neural Stem Cell-Derived Exosomes Facilitate Spinal Cord Functional Recovery After Injury by Promoting Angiogenesis." *Experimental Biology and Medicine (Maywood, N.J.)* 245, no. 1: 54–65.

Zhou, T., Y. Zheng, L. I. Sun, et al. 2019. "Microvascular Endothelial Cells Engulf Myelin Debris and Promote Macrophage Recruitment and Fibrosis After Neural Injury." *Nature Neuroscience* 22, no. 3: 421–435.

Zhou, W., X. Wang, Y. Dong, et al. 2024. "Stem Cell-Derived Extracellular Vesicles in the Therapeutic Intervention of Alzheimer's Disease, Parkinson's Disease, and Stroke." *Theranostics* 14, no. 8: 3358–3384.

Zhou, X., Q. R. Smith, and X. Liu. 2021. "Brain Penetrating Peptides and Peptide-Drug Conjugates to Overcome the Blood-brain Barrier and Target CNS Diseases." *Wiley Interdisciplinary Reviews: Nanomedicine and Nanobiotechnology* 13, no. 4: e1695.

Zhu, L.-P., T. Tian, J.-Y. Wang, et al. 2018. "Hypoxia-Elicited Mesenchymal Stem Cell-Derived Exosomes Facilitates Cardiac Repair Through

20013078, 2025, 7, Downloaded from https://isevjournals.onlinelibrary.wiley.com/doi/10.1002/jev2.70126 by CochraneChina, Wiley Online Library on [27/07/2025]. See the Terms and Conditions (https://onlinelibrary.wiley.com/terms-and-conditions) on Wiley Online Library for rules of use; OA articles are governed by the applicable Creative Commons License

miR-125b-Mediated Prevention of Cell Death in Myocardial Infarction." *Theranostics* 8, no. 22: 6163–6177.

Zhu, Z., Y. Zhai, Y. Hao, et al. 2022. "Specific Anti-Glioma Targeted-Delivery Strategy of Engineered Small Extracellular Vesicles Dual-Functionalised by Angiopep-2 and TAT Peptides." *Journal of Extracellular Vesicles* 11, no. 8: e12255.

Zrzavy, T., C. Schwaiger, I. Wimmer, et al. 2021. "Acute and Non-Resolving Inflammation Associate With Oxidative Injury After Human Spinal Cord Injury." *Brain* 144, no. 1: 144–161.

Supporting Information

Additional supporting information can be found online in the Supporting Information section.

Supplementary Materials: jev270126-sup-0001-SuppMat.docx

20013078, 2025, 7, Downloaded from https://isevjournals.onlinelibrary.wiley.com/doi/10.1002/jev2.70126 by CochraneChina, Wiley Online Library on [27/07/2025]. See the Terms and Conditions (https://onlinelibrary.wiley.com/terms-and-conditions) on Wiley Online Library for rules of use; OA articles are governed by the applicable Creative Commons License